

SCOOP

SAR Altimetry Coastal and Open Ocean Performance

-Algorithm Theoretical Basis Document (ATBD), D1.3 -

Sentinel 3 For Science – SAR Altimetry Studies
SEOM Study 2. Coastal Zone and Open Ocean Study
ESA Contract 4000115382/15/I-BG

Project reference: SCOOP_ESA_D1.5_ATBD
Issue: 1.8

6th April 2020

This page has been intentionally left blank

Change Record

Date	Issue	Section	Comment
24.03.16	1.0		First version
28.07.2016	1.1	2, 3, 4, 5	Updated according to the comments provided by ESA team
20.03.2017	1.2	4,5	Updated according to the comments provided by ESA team, and to match changes to processing schemes.
02/05/2017	1.3	5.1, and 5.4.1.1	Updated last paragraph of section 5.1. Section 5.4.1.1 now includes how f0 and f1 are computed based on the LUT-flag values
02/08/2017	1.4		Document updated according to the changes done in the SAMOSA code (mainly, sections 5.2.5, and 5.4.2.1)
27/09/2017	1.5	5.2.1	Section 5.2.1 updated (mis-pointing geometry)
27/06/2018	1.6	3.2	
12/06/2019	1.7		Updated to include reference to separate SAR L2 ATBD, issued by isardSAT in Feb 2019
06/04/2020	1.8	4	Updated to include information on Coastal Processing

Control Document

Process	Name	Date
Written by:	E. Makhoul-Varona, F. Martin, M. Naeije, P.D. Cotton	24.03.16
Checked by	P. D. Cotton	27.01.20
Approved by:		

	Signature	Date
For SCOOP team		
For ESA		

Table of Contents

Table of Contents	4
1 Introduction	5
2 Overview of algorithms	6
2.1 RDSAR	6
2.2 Doppler stack processing	6
2.3 Echo modelling / retracking	6
3 Algorithm description: RDSAR	7
3.1 Theoretical description, physics of the problem	7
3.2 Algorithm definition: processing steps and mathematical description	9
3.3 Development choices and trade offs	18
3.4 Data flow	18
4 Algorithm description: Doppler stack processing	20
4.1 Theoretical description, physics of the problem	20
4.2 Algorithm definition: processing steps and mathematical description	21
4.3 Development choices and trade offs	38
4.4 Data flow	38
5 Algorithm description: Echo modelling / retracking	41
5.1 Theoretical description, physics of the problem	41
5.2 Algorithm definition: processing steps and mathematical description	42
5.3 Development choices and trade offs	49
5.4 Data flow	49
6 References	63
7 Symbols	66
8 List of acronyms	69

1 Introduction

This is the Algorithm Theoretical Basis Document (ATBD) report for SCOOP and represents D1.3 of the project.

The purpose of this document is to describe the processing schemes that will be applied in SCOOP to generate the test data sets. The first Test Data Set is intended to be a Sentinel-3 “Equivalent” product, to allow an evaluation of the expected performance of Sentinel-3 SAR mode data. Because validated Sentinel-3 data are not available at the time of this phase of the project, the project team will be processing Cryosat-2 FBR data with a Sentinel-3 configuration, to produce the Sentinel-3 “equivalent” product.

Other early project documents: the “State of the Art” (SCOOP TN-1: Cipollini, 2016a), and the Requirements Baseline (SCOOP RB, Cipollini 2016b), provide the scientific background and requirements which contributed to the development and implementation of the processing approaches described in this document

There are 5 further main Sections: Section 2 provide a brief overview of the processing steps, Section 3 provides the Algorithm Description for RDSAR processing, provided by Marc Naeije of TU Delft, Section 4 provides the Algorithm Description for Doppler stack processing, provided by Eduard Makhoul-Varona of isardSAT and Section 5 provides the Algorithm Description for Echo modelling and retracking processing, provided by Francisco Martin of Starlab.

Note that, due to changes in the project team, i.e. the withdrawal of STARLAB from the project, isardSAT took over responsibility for the Echo Modelling and re-tracking for the Phase 2 Test Data Set. A separate ATBD (Makhoul, 2019) has been issued by isardSAT to described this processing.

2 Overview of algorithms

2.1 RDSAR

The main processing stages of the RDSAR processing are:

1. Gather 4 bursts of 64 echoes.
2. Adjust the FAI (Fine Range Word) for each burst.
3. Align the echoes horizontally.
4. Align the echoes vertically (optional).
5. Correct echo amplitude and phase.
6. Zero-pad the echoes.
7. Perform a 1-dimensional FFT (Fast Fourier Transform), horizontally.
8. Incoherently average the individual waveforms.
9. Apply the low-pass filter correction.
10. Rescale the waveform

2.2 Doppler stack processing

The main processing stages of the Doppler-Delay processor (DDP) are:

1. Surface locations, Final burst datation and Window delay
2. Beam angles computation
3. Azimuth processing (Delay-Doppler processing + Stacking)
4. Geometry corrections
5. Range compression
6. Multi-looking
7. Scaling factor computation (sigma0 extraction)

2.3 Echo modelling / retracking

The main processing stages of the Echo modelling / retracking are:

1. Processing configuration parameters.
2. Definition of the main constants.
3. Definition of the starting values for the retracker.
4. Read L1B data.
5. Doppler Beams Computation.
6. Waveform Normalization.
7. Noise Computation.
8. SAR Waveform Fitting.
 - a. A priori parameters set up.
 - b. SAR Waveform Simulation.
 - i. Definition and compilation of the main constants.
 - ii. Computation of the α_p (Point Target Response width) as a function of SWH.
 - iii. Computation of the basis functions.
 - iv. Anti-Aliasing Filter.
 - v. Waveform Computation.
 - c. Execution of the Fitting.
 - d. Storing of the results.

3 Algorithm description: RDSAR

3.1 Theoretical description, physics of the problem

This section describes the theoretical background behind the creation of a Pseudo Low Resolution Mode (Pseudo LRM or PLRM) waveform from CryoSat-2 and Sentinel-3 Synthetic Aperture Radar (SAR) echoes. This conversion technique is also referred to as Reduced SAR (RDSAR).

The reader is referred to relevant documentation from the CP40 and SAMOSA studies for further background and detail (Scharroo, 2014)

CryoSat-2 operates in three different modes: LRM, SAR, and SARin (SAR interferometric mode). The operating modes are switched at the edges of a predetermined mode mask (see Figure 3.1-1) such that it will operate in a given mode in a given geographical area. The mode mask is regularly updated to include the changing of ice sheets. Generally, CryoSat-2 is operating in LRM mode over most of the oceans, SAR over some coastal areas and a few selected boxes in the open ocean, SARin over the edges of ice shelves and mountain glaciers.

LRM is the classical mode used by all historical radar altimeters, pulsing between 2000 and 4000 times per second. The pulse interval is large enough that the returned echoes are uncorrelated and no SAR technique can be applied. CryoSat-2 is the first radar altimeter to also provide a SAR mode, transmitting pulses at a much higher frequency (18 kHz) but only one third of the time, waiting two thirds of the time to receive the echoes (Figure 3.1-2).

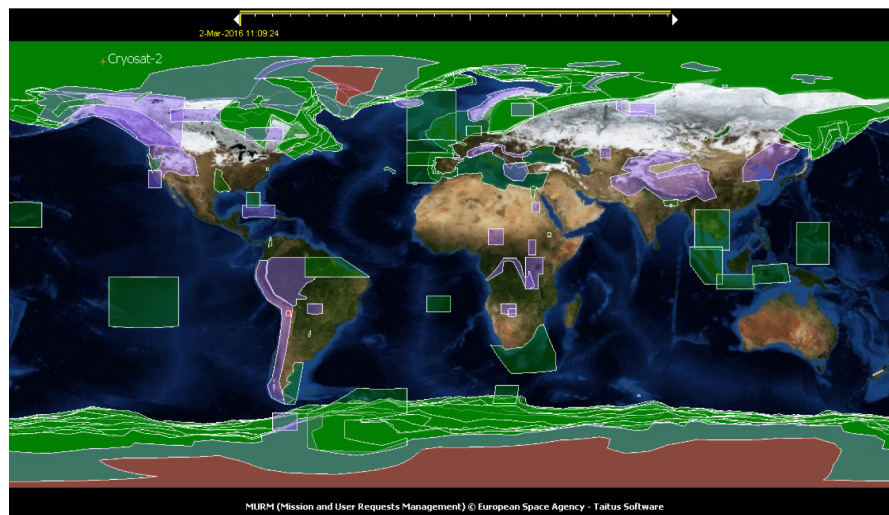


Figure 3.1-1 The current CryoSat-2 mode mask (version 3.8). Green is SAR mode, purple is SARin mode, and other areas are in LRM mode.

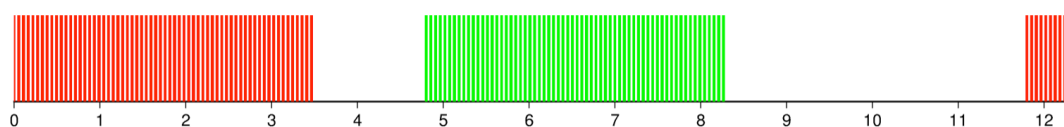


Figure 3.1-2 Illustration of one burst of pulses (red) and reception of their echoes (green). The total burst duration is 11.8 ms.

The processing of the SAR echoes is significantly different from the traditional LRM mode. In the first case the complex echoes are averaged coherently: their phase is taken into account when summing the complex echoes. In the second case the echoes are averaged incoherently: their phase is not taken into account when summing just the power of the echoes. The intent of the RDSAR technique is to create waveforms that look like LRM mode waveforms but are not that entirely because in SAR mode the instrument is not transmitting at a constant rate but has this two-thirds waiting time as mentioned before. This explains the name Pseudo LRM waveforms.

For the creation of these Pseudo-LRM (PLRM) waveforms we have to go back to the Level 1A product known as FBR (Full Bit Rate). That product holds all the echoes that are received in complex form. The resulting waveforms can be regarded a Level 1B product, similar to standard LRM Level 1B products.

The PLRM data have been merged with LRM data and have been available via RADS (<http://rads.tudelft.nl>) since October 2012. Since then, NOAA has developed other techniques to process the SAR data, taking advantage of the higher spatial resolution it can provide.

The processing of the CryoSat-2 LRM and PLRM data will follow exactly the steps as done in RADS frame, as done by NOAA/EUMETSAT within and outside the framework of the CP4O project: these have been reported at various meetings and in various publications (Scharroo et al. [2012a, b,c,d,e], Scharroo et al. [2013a,b], and Smith and Scharroo [2014]).

The processing of the Sentinel-3 RDSAR and PLRM data will not deviate from the methods adopted for the CryoSat-2 data processing. The instrument also makes use of the unfocused SAR with closed burst meaning that there are bursts of pulses and no continuous pulses at exactly the same frequency as CryoSat-2 (bursts of 64 pulses, though flanked with 2 C-band pulses - Figure 3.1-3).

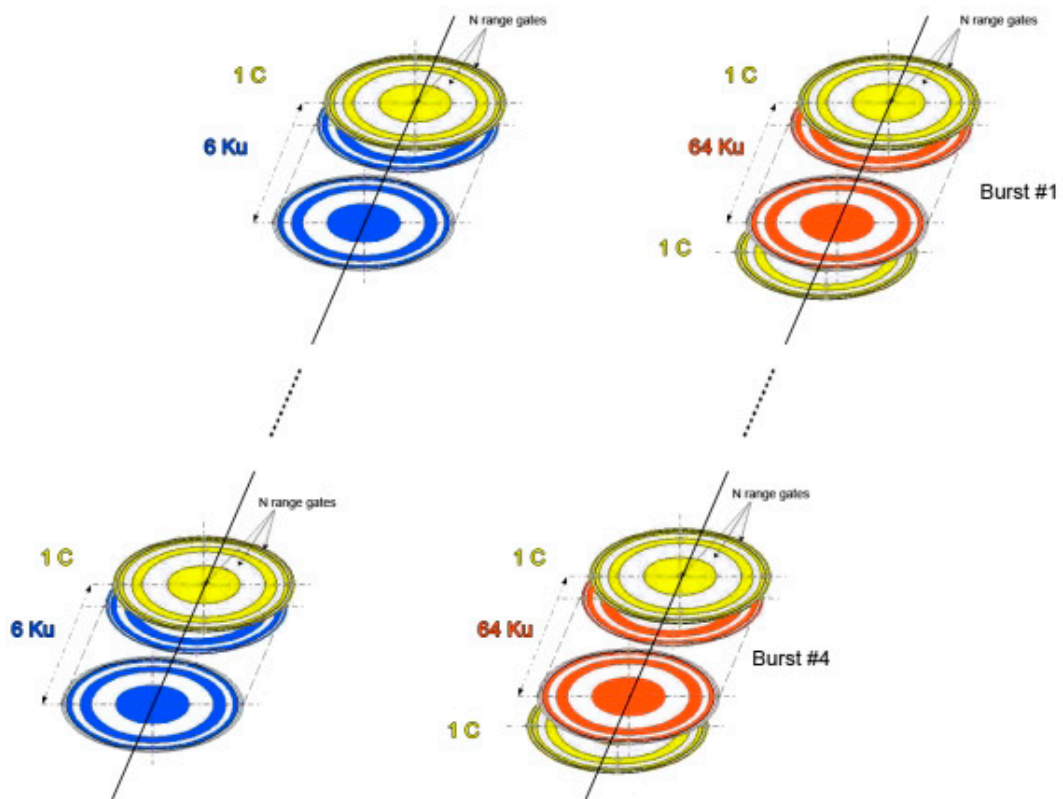


Figure 3.1-3 Sentinel-3 LRM radar cycle transmitting pattern (left) and SAR radar cycle transmitting pattern (right). However, the LRM mode was dismissed. SAR radar cycles contain four bursts, each of these bursts have sequences of 1 C - 64 Ku - 1 C pulses. (Thales Alenia Spazio).

3.2 Algorithm definition: processing steps and mathematical description

The RDSAR technique comprises the following steps, starting with the L1A FBR product:

1. Gather 4 bursts of 64 echoes.
2. Adjust the FAI for each burst.
3. Align the echoes horizontally.
4. Align the echoes vertically (optional).
5. Correct echo amplitude and phase.
6. Zero-pad the echoes.
7. Perform a 1-dimensional FFT, horizontally.
8. Incoherently average the individual waveforms.
9. Apply low-pass filter correction.
10. Rescale the waveform.

These steps are described in more detail in the next section, and Figure 3.2-1 illustrates the overall process. The results are 20-Hz waveforms similar to those found on the so-called L1B LRM products. After that the PLRM data can be processed to L2 as if they were real LRM data (however with some caveats), and the range (satellite – sea surface distance) can be computed. This is explained in the subsequent section.

Since the power of the waveforms is scaled such that the maximum value for any sample is always 65535, a detailed description of the power amplification is given in the Power Conversion section.

The equations given in Sections 3.2.1 until 3.2.3 (Equations 3.2.1 up to and including 3.2.17) come from the RADS RDSAR processing, which was setup by Remko Scharroo and Walter Smith (both at NOAA at the time). The first full description of the algorithm including the used equations can be found in Scharroo, 2014.

3.2.1 Algorithm definition PLRM waveforms

3.2.1.1 Gather 4 bursts of 64 echoes

During every 20-Hz radar cycle, CryoSat-2 and Sentinel-3 produce 4 bursts. Each burst lasts about 3.5 ms, in which 64 Ku pulses are produced at a frequency of about 18 kHz. After a waiting period to receive the echoes, the next burst starts at 11.8 ms intervals (Figure 3.1-2).

The FBR data contain during each 20-Hz cycle, 4 sets of 64 echoes, each containing 128 complex (I and Q) samples. These echoes from the FBR data have already been de-ramped in the time domain but are not yet been calibrated (at least for CryoSat-2, Sentinel-3 FBR may contain calibrated data but that is still to be decided because that would mean a much larger dataset). This means that the power of the echoes is relative to the gain settings and the phase is determined by the location of the range window. But neither the gain nor range window delay has been calibrated for instrumental effects.

The 4 bursts are individually time tagged and geo-located in the FBR product. To produce the referencing of the final 20-Hz PLRM waveforms, the time in between the second and third burst is computed. The geo-location of the 20-Hz sub-satellite point and altitude is then computed by interpolating the satellite orbit. The FBR products always contain all four bursts per radar cycle, so there are no complexities when they are not all 4 available.

3.2.1.2 Adjust the FAI for each burst

The position of the waveform leading edge is kept close to the sample 34 (counting from 0 to 127) by the on-board tracker. The uncorrected window delay is given by the coarse range word (LAI), which has a digitisation of 4 range gates. In addition, the tracker gives an estimate of how far the waveform leading edge will be displaced from the optimal position, known as the fine range word (FAI), which has a range of -128 to 127 and is equivalent to ± 2 range gates.

The tracker is noisy and has a tendency to mis-estimate the range rate. When the on-board tracker is producing a higher or lower rate than the actual rate of change of the range, the waveform will be blurred. Over oceans, the altitude rate is a better approximation of the range rate than the one suggested by the on-board tracker. Hence, we will adjust the FAI estimates such that they will be in accordance with the altitude rate, while taking into account that the LAI may change between bursts.

Say that LAI (the uncorrected window delay in units of range), FAI (in units of range), and the orbital altitude h are arrays of four elements, one for each burst in a radar cycle. Then the array FAI is recomputed as follows (Equation 3.2-1):

$$\text{FAI} = (\overline{\text{LAI} + \text{FAI}} - h + h - \text{LAI}) \quad \text{Eq. 3.2-1}$$

where the over-line denotes the average over the four elements of the arrays.

3.2.1.3 Align the echoes horizontally

The complex power for each of the samples (bins) for each echo within a burst is given a phase shift equivalent to the change of range compared to the new 20-Hz time tag. Here we have to distinguish both the change of range between the bursts given by the adjusted FAI from the previous processing step and the change of range within a burst. In both cases the change of range is based on the altitude rate rather than the on-board tracker information. However, we do take here into account (in the adjusted FAI numbers) that the LAI may change between bursts.

The phase shift ϕ to be applied to sample k (running from 0 to 127) of echo p (running from 0 to 63) is the sum of three components (Equation 3.2-2):

$$\phi = (k - 63.5)\phi_k + \phi_d + \phi_c \quad \text{Eq. 3.2-2}$$

where ϕ_k is the phase advance between samples, which in turn is determined by 2-way time delay, τ_{FAI} associated with the change in adjusted FAI (the change of range *between* the bursts) and the 2-way time delay associated with the change of range *within* a burst, τ (Equation 3.2-3):

$$\phi_k = (\tau_{\text{FAI}} + \tau)\omega_k \quad \text{Eq. 3.2-3}$$

where τ_{FAI} is determined by the adjusted FAI, τ depends on the pulse number p , the altitude rate \dot{h} , the time between pulses (55 μs), and ω_k is the frequency change between samples (Equations 3.2-4 - 3.2-7):

$$\tau_{\text{FAI}} = 2 \text{ FAI}/c \quad \text{Eq. 3.2-4}$$

$$\tau = (2p - 63)\tau_p \quad \text{Eq. 3.2-5}$$

$$\tau_p = \dot{h}(55\mu\text{s})/c \quad \text{Eq. 3.2-6}$$

$$\omega_k = -2\pi/(400\text{ns}) \quad \text{Eq. 3.2-7}$$

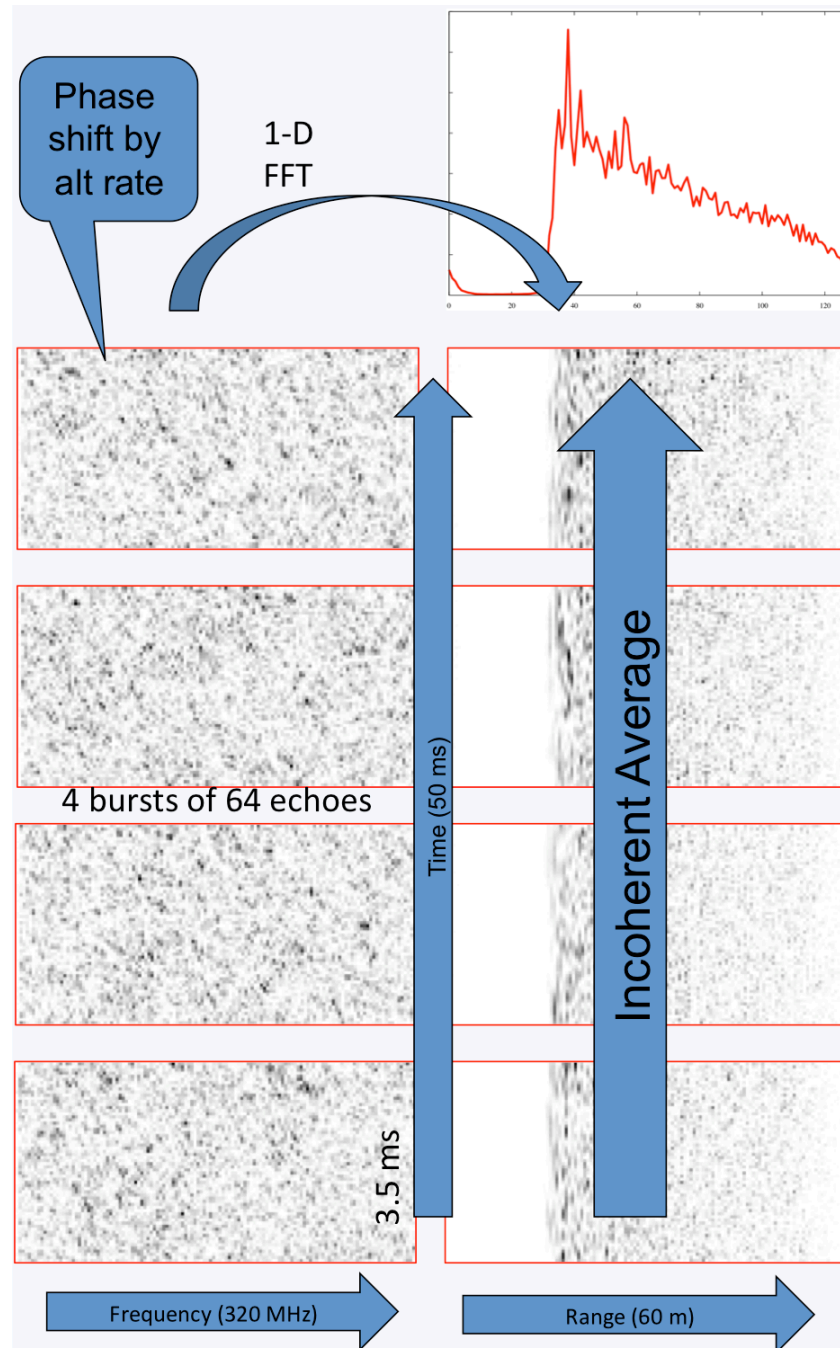


Figure 3.2-1 Four bursts of 64 complex echoes (left) are phase shifted so that after 1-D FFT the individual waveforms are all aligned (right). Those waveforms are then incoherently averaged to form a single 20-Hz PLRM waveform. Zero padding is not shown. Of the echoes and individual waveforms only the power is shown, not the phase, however each are built of complex numbers.

3.2.1.4 Align the echoes vertically

An additional (but not essential) step in the echo alignment is the phase shift ϕ_d in Eq 3.2-2

This shift is intended to align the echoes "vertically", meaning that after a 2-dimensional FFT the peak power will be in the nadir Doppler bin. This "Doppler shift" equals

$$\phi_d = 2\pi f\tau$$

Eq. 3.2-8

where f is the radar frequency of 13.575 GHz. Figure 3.2-2 shows a single burst converted by a 2-dimensional FFT. Because we will actually perform a 1-dimensional FFT, this step is not essential and has no impact on the final waveform obtained.

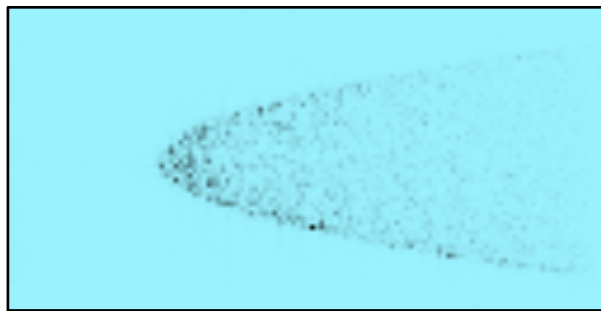


Figure 3.2-2 A single burst after 2-dimensional FFT. The peak power is aligned vertically such that it falls on the nadir Doppler bin.

3.2.1.5 Correct the echo amplitude and phase

Because the altimeter power and phase are not entirely stable (constant) during a burst, each of the 64 pulses (echoes) within a burst needs its amplitude and phase to be corrected. The amplitude factors (increasing from the first pulse to the last, with an average of 1) and phase shifts (starting with a zero phase shift and increasing with increasing pulse number) are retrieved from the IPFDB file `CS_OPER_AUX_IPFDBA_20101111T101900_99999999T999999_0002.EEF`. The phase shift ϕ_e is one of the three components in Eq 3.2-2.

3.2.1.6 Zero-pad the echoes

Zero-padding is a technique used to minimise the loss of information when performing the subsequent 1-dimensional FFT and incoherent averaging. This loss of information and its remedy was proposed by *Jensen* [1999] and was only proven to be actually beneficiary by *Smith and Scharroo* [2014] based on the processing of CryoSat-2 FBR data.

Zero-padding is obtained by adding 64 (complex) zeroes on each side of the 128 bins of complex echoes. This is because the zero frequency is in the middle of the 128 bins, and negative and positive frequencies run to the left and right respectively. The extra 64 (complex) zeroes simply suggest zeroes at higher negative and positive frequencies.

3.2.1.7 Perform a 1-dimensional FFT, horizontally

Each of the 64 pulses in 4 bursts is now individually FFT'd. This results in 256 very noisy "individual waveforms" of 256 complex samples each, as illustrated in the right column in Figure 3.2-1. Note that the "leading edge" of the each of these "waveforms" is properly aligned on the tracking gate (34).

3.2.1.8 Incoherently average the individual waveforms

The 256 "individual waveforms" are incoherently averaged (in fact, they are summed in our implementation). This means that each sample k of the resulting 20-Hz PLRM waveform is determined by summing the power across the 256 "individual waveforms":

$$W(k) = \sum_{p=0}^{255} [I(p, k)^2 + Q(p, k)^2] \quad \text{Eq. 3.2-9}$$

where $W(k)$ is the waveform power for each sample (k runs from 0 to 255) and $I(p, k)$ and $Q(p, k)$ are the complex samples of the individual waveforms after FFT.

3.2.1.9 Apply the low-pass filter correction

The individual samples of the resulting waveform need to be adjusted in power to correct for the effect of the low-pass filter (LPF) used to separate the de-ramped signal after differencing the received radar echoes with a duplicate of the transmitted pulse. Because this differencing also creates a signal with the frequencies summed, an LPF filter is used to extract only the lower (differenced) frequency.

However, the LPF filter has imperfections that result in a change in effective power from one sample to the next. This is characterised by the CAL2 calibration and the results are available in the IPFDB. Because the LPF correction appears to be constant, we use the values from IPFDB file CS_OPER_AUX_IPFDBA_20101111T101900_99999999T999999_0002.EEF.

In order to correct the 256 samples, we have obtained after zero-padding, we expanded the LPF correction table from 128 to 256 samples by means of linear interpolation.

3.2.1.10 Rescale the waveform

The waveforms are rescaled such that the highest value for any sample in a waveform is always 65535. The way to compute the proper power from these waveforms is described in Section 3.2.3.

3.2.2 Range computation

The PLRM range measurement can be determined by adding the estimated epoch of the leading edge of the waveform (converted to units of range) to the tracker range. In other words:

$$\text{range_20hz_ku} = \text{range_tracker_20hz_ku} + r \quad \text{Eq. 3.2-10}$$

where

- range_20hz_ku is the total calibrated one-way range provided on the RADS PLRM products.
- $\text{range_tracker_20hz_ku}$ is the tracker range relative to gate 34 (starting from 0), corrected for USO drift, Doppler correction and internal calibration, as given on the RADS PLRM products.
- r is the range correction determined by the tracker, giving the position of the leading edge relative to gate 34.

3.2.3 Power conversion

In the RADS PLRM data provided in the framework of the ESA funded CP4O project, with each PLRM waveform a scale factor is provided. This scale factor is computed as follows (Eq. 3.2-11):

$$G = -G_W - G_{TxRx} - G_{S,SAR} - G_{AGC} - G_{Tx} - G_N \quad \text{Eq. 3.2-11}$$

where

- G is the waveform scale factor in dB; this is stored as variable `waveform_scale_20hz` on the PLRM product.
- G_W is the scale factor needed to normalise the PLRM waveforms as discussed in Section 3.2.1.10, expressed in dB.
- G_{TxRx} is the transmitter and receiver gain provided on the L1A product (in dB).
- $G_{S,SAR}$ is the processor gain in SAR mode. Theoretically, $G_{S,SAR}$ is 126.227 dB, but comparing LRM to PLRM leads to 125.8 dB, which value we have used.
- G_{AGC} is the AGC setting, properly corrected from integer values (in dB).
- G_{Tx} is the transmitted power (in dBW).
- G_N is the nominal attenuation at nominal altitude ($h_N=735$ km) and with zero off-nadir angle ($G_N=-151.125$ dB).

In order to compute the backscatter coefficient σ_0 from the waveform scale and other parameters, add the following components (Eq. 3.2-12):

$$\sigma_0 = G + G_{amp} + G_\eta + G_h + G_\xi + G_{SWH} \quad \text{Eq. 3.2-12}$$

where

- σ_0 is the backscatter coefficient; this is stored as variable `sig0_20hz_ku` on the RADS PLRM products.
- G is the waveform scale factor, expressed in dB, as defined in Eq 3.2-11 above.
- G_{amp} is the amplitude determined by the re-tracker based on the waveforms normalised to have a peak value of 65535, converted to dB. This means that the values are generally around 48 dB ($10 \log_{10}(65535)$).
- G_η is an attenuation correction for the flattening of the Earth, then converted to dB (Eq. 3.2-13):

$$G_\eta = 10 \log_{10} \left(\frac{1+h/R}{1+h_N/R} \right) \quad \text{Eq. 3.2-13}$$

where h is the orbital altitude, h_N is the nominal altitude (735 km), R is the mean radius of the Earth (6371 km). The absolute value of this correction is generally smaller than 0.01 dB.

- G_h is the attenuation because of non-nominal altitude, converted to dB (Eq. 3.2-14):

$$G_h = 30 \log_{10}(h/h_N) \quad \text{Eq. 3.2-14}$$

- G_ξ is the attenuation because of off-nadir angle, ξ , expressed in dB (Eq. 3.2-15):

$$G_\xi = \frac{40\xi^2}{\gamma \ln 10} \quad \text{Eq. 3.2-15}$$

- G_{SWH} is the attenuation because of the SWH, expressed dB. However, this is very small (order of 0.001 dB) and can be handily ignored.
- γ is an antenna aperture parameter based on the full beam width β of the antenna, such that

$$\gamma = \frac{2}{\ln 2} \sin^2 \frac{\beta}{2} \quad \text{Eq. 3.2-16}$$

- β is the (weighted) beam width of the elliptical CryoSat-2 antenna, whose square is determined by the harmonic mean of the square of the along-track and cross-track beam widths (1.10° and 1.22°, respectively) (Eq. 3.2-17):

$$\beta^2 = \frac{2}{1/\beta_1^2 + 1/\beta_2^2} \quad \text{Eq. 3.2-17}$$

3.2.4 From PLRM waveforms to PLRM range, swh and σ_0

The RADS implementation of processing the PLRM waveforms (level 1b) into a range product (level 2) applies a 3-parameter estimation to the waveforms (radar echoes), *i.e.*, range (epoch), swh (width/gradient), and wind (amplitude). This is referred to as MLE3, where MLE stands for maximum likelihood estimator. However, we also compensate for the mispointing of the antenna, by using information from the on-board star trackers (off-nadir angle). Actually, this makes the RADS implementation similar to an MLE4, only that the 4th parameter is not estimated from the waveform (decay) itself. Mispointing can have a significant influence on the performance of the altimeter instrument. If the off-nadir angle is zero or very small a straightforward MLE3 would be the preferred re-tracker for open ocean, but for the CryoSat-2 platform it cannot be neglected. Smith and Scharroo [2011] provides more detail on the retracking of range, SWH, sigma0, and attitude in CryoSat-2 LRM altimetry and how it is done in RADS: here the CS2's waveforms from the ESA L1b FDM and LRM products have been retracked based on circular beam theory using the azimuthally averaged Half Power Beam Width. This seems to work pretty well as an approximation for the LRM waveforms (in fact the antenna pattern is slightly elliptical). Parameters that are re-tracked are epoch, width, amplitude, mispointing and noise. Basically, the system allows for choice of parameters to be fit and parameters to be held fixed, but the MLE4 approach, as mentioned before, where the 4th parameter (mispointing) does not actually come from the fit but from the given off-nadir angle, is highly favoured. For the processing of the PLRM waveforms we follow exactly the same approach.

3.2.4.1 Re-tracking the waveforms

Figure 3.2-3 provides the quantities to derive from the mean waveform: they are directly linked to range, swh, and backscattered power (thus indirectly wind speed).

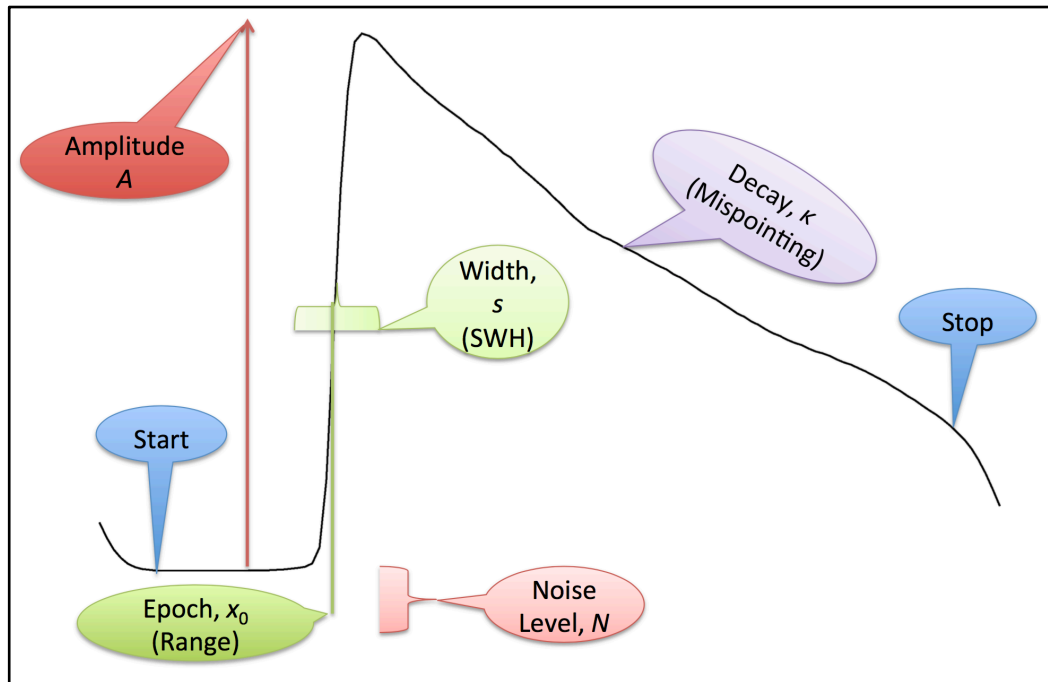


Figure 3.2-3 Estimated parameters from an open ocean waveform (Smith and Scharroo, 2011).

As the classical ‘Brown model’ for fitting a curve through the open ocean waveform assumes a circular antenna pattern and knowing that the antenna pattern for CryoSat-2 is slightly elliptical we average CryoSat-2 beam width over all azimuths then the azimuthally averaged half-power beam width (HPBW) is the harmonic mean of the major and minor elliptical HPBWs. We re-track the CryoSat-2 waveforms with a circular beam theory using this approximation, which is allowed for conventional LRM waveforms (Amarouche et al., 2004).

The RADS re-tracker as developed by Walter Smith from NOAA (Smith and Scharroo [2011]) allows selection of any (or all) of these parameters to be fitted:

1. Epoch, x_0
2. Width, s
3. Amplitude, A
4. Mispointing, $k(\xi^2)$, ξ is off-nadir angle
5. Noise level, N

and any of these can be free parameters to be fitted, while others are held fixed. $k(\xi^2)$ can use 0th, 1st or 2nd order approximation of Bessel function $I_0(z)$:

- 0th Order: $I_0(z) = 1$ Approximates $I_0(B*\sqrt{t})$ as 1 (MacArthur, 1978)
- 1st Order: $I_0(z) = \exp(z^2/4)$ Approximates $I_0(B*\sqrt{t})$ as $\exp(-B*B*t/4)$ (Rodriguez, 1988)
- 2nd Order: $I_0(z) = \text{two terms in exp}()$ Approximates $I_0(B*\sqrt{t})$ as $2*\exp(-B*B*t/8)$ (Amarouche et al., 2004)

For instance an MLE3 would be the fit of the first three parameters and a 1st order approximation, an MLE4 the fit of the first four parameters and a 2nd order approximation, and a so-called RED3 would be the fit of the first 3 parameters, a 1st order approximation and fewer gates fitted. The solution chosen for RADS is an MLE3 with a fixed (a priori) ξ from the platform attitude found from star trackers which data is given in the ESA FDM and LRM 1b products. However, it appeared necessary to deal

with platform attitude biases in pitch and roll, which have been established fitting a bias model (Eq. 3.2-18):

$$\xi^2 = (\text{pitch} - \text{bias}_p)^2 + (\text{pitch} - \text{roll})^2 \quad \text{Eq. 3.2-18}$$

Here we neglected thermal flexures and any biases between the star trackers. The pitch bias was estimated at +0.0962° and the roll bias at +0.0848° (Smith and Scharroo, 2011)

3.3 Development choices and trade offs

Though the idea of the project is to prepare for Sentinel-3 and process the data ‘as if they were’ from Sentinel-3, we more or less stick to CryoSat-2 implementation as close as possible. For starters, in the RDSAR procedures themselves nothing will change significantly as nothing significantly changed in the instrument and/or sampling. CryoSat-2 and Sentinel-3 are both closed burst systems with a waiting period to receive the bursts (non-interleaved) and even the implementation is almost identical (burst of 64 Ku-band pulses, be it for Sentinel-3 surrounded by 2 C-band pulses). This will provide a small change in the timings but we cannot pretend to have these C-band pulses when processing CryoSat-2 data.

There are some other differences that impact the results maybe but not the implementation. Sentinel-3’s antenna pattern is circular so indeed can we use the standard re-tracking methods (preferably MLE3 with off-nadir angle from star trackers, which will be smaller for Sentinel-3).

Also, the availability of calibrated FBR, which actually is not certain for Sentinel-3 would not really change the processing but only make it a bit simpler, skipping 2 steps, and by that faster.

3.4 Data flow

3.4.1 Input data

As input for our processing chain we will use the newly provided FBR data for all the SCOOP regions of interest (ROIs), as they will be supplied by ESA to isardSAT (including calibration files). Redistribution will be by means of hard disks because the data volume is just too big to have it downloaded through an ftp server.

3.4.2 Ancillary information

To fill the remainder of fields in the to be produced RADS RDSAR NETCDF files the RADS standard will be followed (including the ‘best’ and most up-to-date models and corrections) and maybe other auxiliary data can be included which has to be decided on. It is clear that when use is made of uncalibrated FBR that CAL1 and CAL2 information will be needed.

3.4.3 Output

TU Delft will produce the PLRM products based on the described RDSAR procedures for all the SCOOP ROIs. These will have two flavours, one with the 20Hz mean (PLRM) waveforms, so that

users can use their own re-tracker software if preferred, and one without the waveforms for those who do not need the waveforms and/or want a more manageable dataset. Both products though will carry the final 20-Hz and 1-Hz data (level 2) and are put in NetCDF format (no compression) according to the RADS (version 4) definitions. The reader is also referred to similar products that were produced in CP40 frame. To read the data it would be handy to install the RADS code but this is not mandatory as NetCDF data are self-explanatory (e.g., using `ncdump`). The data will be divided over passes, where a pass is half an orbit and extending from the most southern measurement to the most northern and vice versa. Pass definition comes from the definition adopted in RADS for CryoSat-2: due to the large repeat cycle we have subdivided these into smaller cycles of 29 days, the chosen sequence of revolutions is $4 * (29 + 29 + 27) + 29 = 369$ days. With this definition, e.g., cycle 10 starts YYMMDDHHMMSS.sss=101219165257.140.

There will be one file per pass, indicated by `c2pPPPPcCCC.nc`, where PPPP indicates the pass number and CCC the cycle number. The re-tracking is done as described in the previous sections with the suggested zero-padding of the waveform.

The geophysical corrections are all 1-Hz, and the measurements (corrected for instrumental drift and biases) are given both at 20-Hz and 1-Hz. The data is produced as per the RADS standards. All that is different from e.g. Jason products is:

- Different variable names and attributes like scale and offset, though these are obvious given the description in the attributes.
- Ocean tide DOES NOT include the load tide, so you will have to apply both. This is for historical reasons, and because it makes a more logical division between land and ocean.
- The MOG2D correction is the TOTAL Dynamic atmospheric correction (DAC), not just the high-frequency part, as the division between high and low is arbitrary.

What is added as well, is the “ssha” (and “ssha_20hz”). These are the 1-Hz (and 20-Hz) Sea Surface Height Anomaly (SSHA) after all corrections and editing have been applied.

Depending on what is decided on what will be (extra) auxiliary data in the data files, the anticipated data volume for RDSAR PLRM 20Hz data is ≈ 500 Mb/cycle for PLRM_no_wvf and ≈ 5 Gb/cycle for the PLRM_with_wvf. A cycle being 29 days this makes roughly 6 Gb and 60 Gb per year for all SAR areas.

4 Algorithm description: Doppler stack processing

4.1 Theoretical description, physics of the problem

The Delay-Doppler altimeter uses the power backscattered from the scene more efficiently than does the conventional altimeter, since the whole beam-limited along-track signal is exploited, instead of the pulse-limited area typically considered by conventional altimeters, as schematically sketched in Figure 4.1-1. This is achieved thanks to the proper slant range (or delay) variation compensation. The extra delay observed from each Doppler bin in which the along-track beam is partitioned is removed, aligning all the Doppler beams to the same delay or range, known as range migration correction (RMC, see Figure 4.1-1).

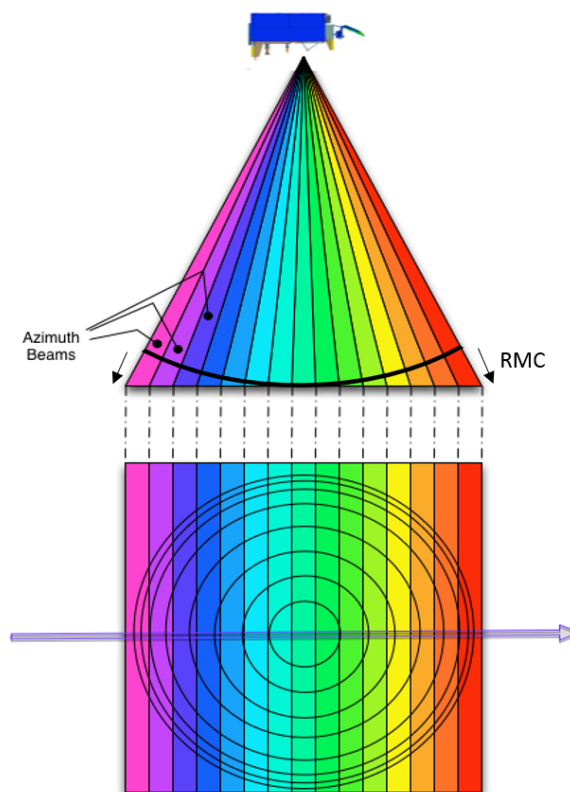


Figure 4.1-1 Delay-Doppler altimeter's illumination geometry side (top) and footprint (bottom) plan views. The along-track beam is partitioned in several Doppler beams with improved resolution. An extra delay or range per beam needs to be compensated, by introducing the range migration correction-RMC (credit: ESA).

The additional selectivity in the Doppler domain, which confers an additional degree of freedom, allows increasing the along-track resolution (i.e., reducing the along-track footprint), such that the impact of terrain variability on the imaged footprint can be minimised. Such improved resolution can be appropriately exploited for coastal altimetry, providing improved performance mainly due to the reduced land contamination as stated in Gommenginger et al. 2013.

This selectivity in the Doppler dimension can be also exploited to perform a specific focusing to a given defined location. This requires to perform additional processing in the along-track direction, which mainly consists on beam steering (to the desired surface position) and Fourier transformation.

In this manner, several looks are made available for a specific surface position, i.e., different Doppler beams from different bursts are pointed towards it, forming the Doppler stack, as exemplary shown in Figure 4.1-2. Therefore, the final signal-to-noise ratio (SNR) can be improved once the different range-compressed power waveforms are incoherently accumulated; such processing is known as multi-looking.

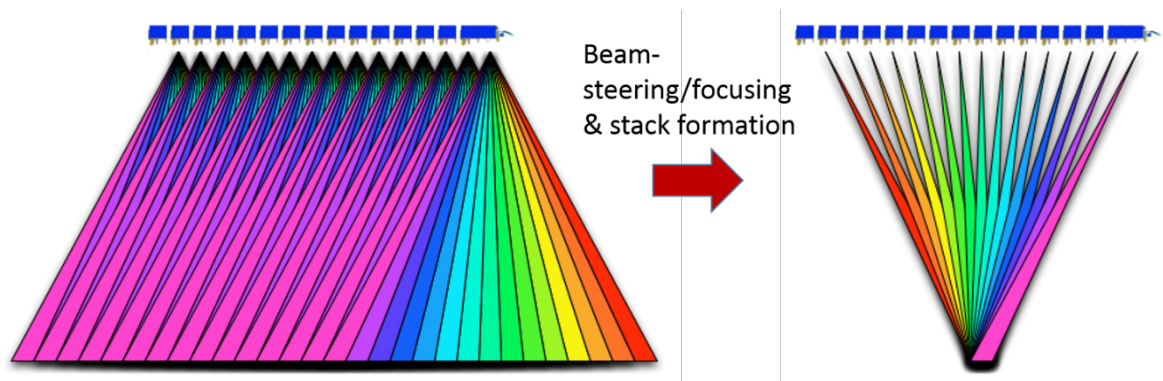


Figure 4.1-2 Conceptual representation of beam-steering processing and stack formation for a given surface (credit: ESA).

Hence, the intrinsic 2-D (range/Doppler) nature of the Delay-Doppler altimetric signals requires, as theoretically described above, to perform accordingly a 2-D processing, properly exploiting the potential capabilities, conferred by this relatively new operational mode.

4.2 Algorithm definition: processing steps and mathematical description

In the following lines, the proposed Delay-Doppler processor baseline to be implemented within the SCOOP project is presented, defining the different algorithms and processing steps included, as well as their rational mathematical description. The potential improvements are also defined in this description.

The considered SAR (aka Delay-Doppler) processor is based on the experience gained by isardSAT in the study and implementation of the Ground Prototype Processor (GPP) within the Sentinel-6 project¹.

The main processing stages of the Doppler-Delay processor are:

- a. Surface locations, Final burst datation and Window delay computation
- b. Beam angles computation
- c. Azimuth processing (Delay-Doppler processing + Stacking)
- d. Geometry corrections
- e. Range compression
- f. Multi-looking
- g. Scaling factor computation (sigma0 extraction)

¹ The Sentinel-6 Algorithm Technical Baseline Description (ATBD) is a reference for all the methodologies applied in the L1 processing. This document is still internal to the S6 project but will be ready before the conclusion of this project

The corresponding flow chart of the proposed Doppler-Delay processor is represented in Figure 4.2-1

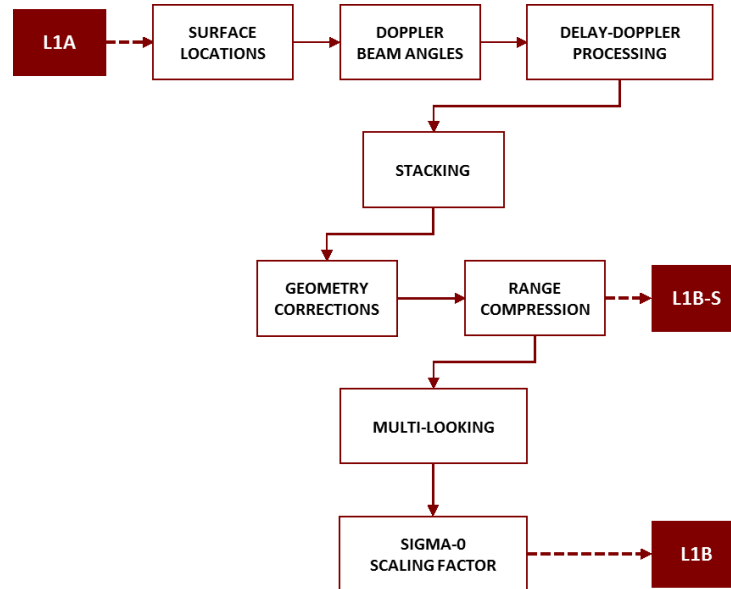


Figure 4.2-1 Level-1A/Level1-B SAR processing chain (credit: isardSAT). For details on the input/output data levels description, please refer to section 4.4.

4.2.1 Surface locations, surface datation and window delay Computation

4.2.1.1 Purpose and scope

The aim of this algorithm is to compute the surface locations (and their corresponding datation and orbit parameters) defined by the intersection of the Doppler beams and the estimated surface positions along the satellite track. The block diagram of the processing flow for this algorithm is depicted in Figure 4.2-2.

4.2.1.2 Mathematical description

The first surface location is determined by the window delay associated with the first burst of the tracking cycle. Then, an iterative process starts and lasts until the end of the orbit data is reached. This process goes through the following steps:

- Computation of angular Doppler resolution: This is obtained at the current satellite position given the Doppler frequency expression (Cumming and Wong, 2005):

$$f_d = \frac{2|\vec{v}_s| \cdot \sin \theta}{\lambda} \quad \text{Eq. 4.2-1}$$

where $|\vec{v}_s|$ is the satellite velocity vector and λ the carrier wavelength. As the azimuth processing will give a Doppler frequency sampling given by the inverse of the burst duration τ_B , the angular azimuth beam resolution is calculated as:

$$\theta = \arcsin\left(\frac{\lambda}{2|\vec{v}_s| \cdot \tau_B}\right) \quad \text{Eq. 4.2-2}$$

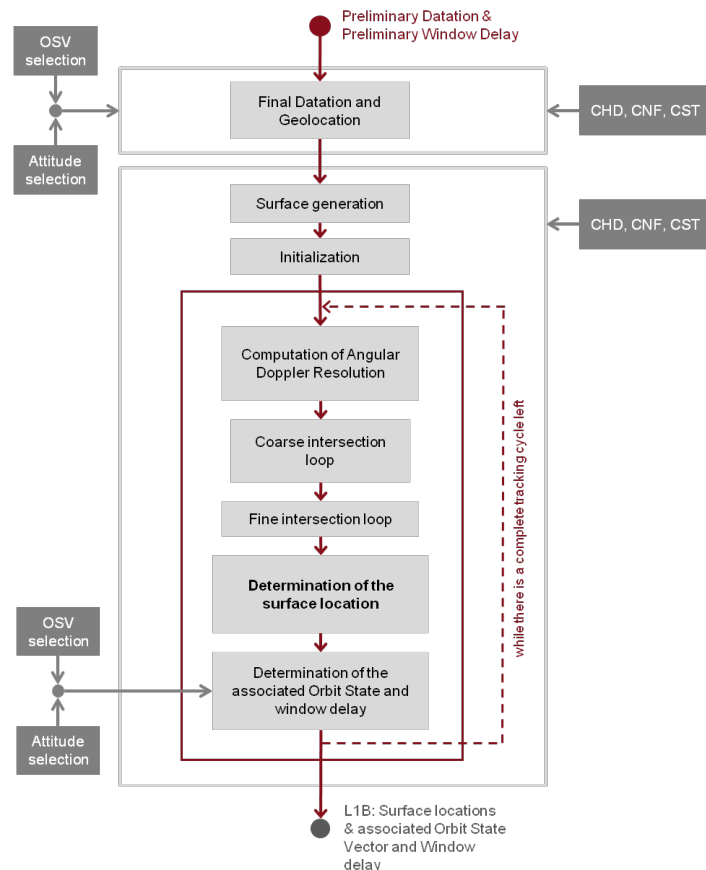


Figure 4.2-2 Surface Locations algorithm's flow chart (credit: isardSAT): OSV stands for (orbit state vector), CHD, CNF and CST refer to the characterization, configuration and constants files, respectively (please refer to section 4.4).

- **Coarse and fine intersection loops:** Determine the intersection between the direction defined by the angle θ_j (angular azimuth beam resolution) with respect to the nadir and each surface location. This process is performed by iterating through the surface positions until the angle of sight α_i^2 is bigger than the angular azimuth beam resolution θ_j (j being the current surface index), see Figure 4.2-3 on the left. Then an interpolation is performed between the last angle of sight and the previous one. After that, a second iteration process starts (the fine intersection loop) and finishes when the angle of sight coincides with the angular azimuth beam resolution (Figure 4.2-3, right).

² A given angle of sight α_i is the angle between the nadir direction and the vector determined by the satellite position above the current surface and the i th burst surface position (i.e., the position of the satellite for the i th burst projected on-ground). Then, each α_i is computed for the consecutive bursts position on-ground until this angle is bigger than θ_j , at most up to 5 values of α_i will be computed since, as a rule of thumb, between a pair of consecutive surface locations up to 4 bursts (1 radar cycle) will be transmitted.

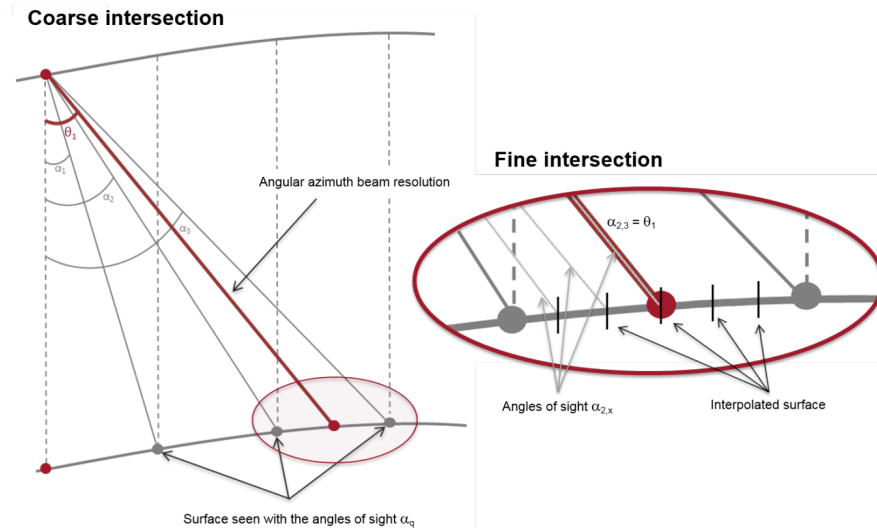


Figure 4.2-3 Coarse (left) and fine (right) intersection step of the surface locations algorithm (credit: isardSAT): α_i corresponds to the angle of sight (between the nadir direction and the vector from satellite position to each burst surface position) and θ_j is the angular/beam Doppler resolution for the j -th surface.

- **Determination of the associated orbit state and window delay:** The associated orbit state can be retrieved using orbit interpolators or libraries. If not available, the orbit can be manually interpolated. Then, the new surface location is also located on the orbit (this would be the action of going from the surface to the orbit and it is represented in Figure 4.2-4 with the red lines going from the surface locations to the orbit). In addition, the window delay of the new surface location is calculated. Then, the obtained state vector is stated as the new one and the iteration process starts again (in Figure 4.2-4 each red point on the orbit is a new point of start).

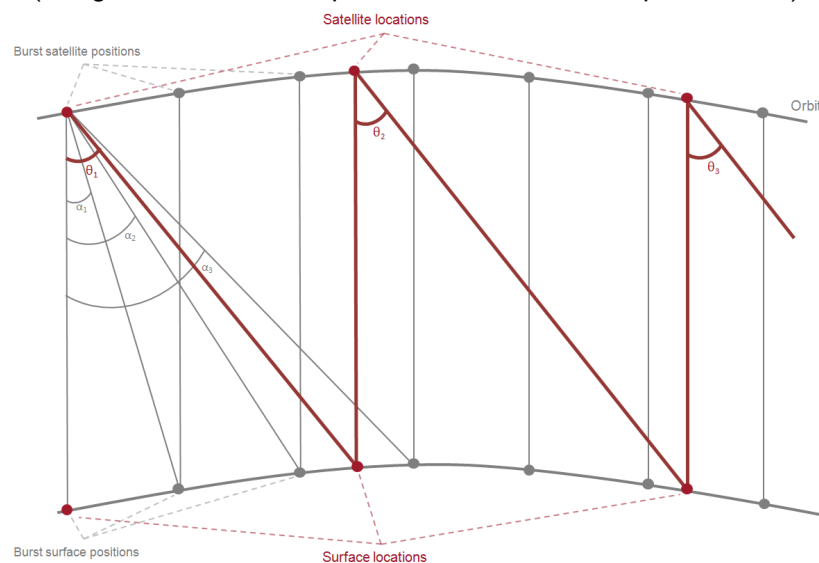


Figure 4.2-4 Determination of the associated orbit state and window delay (credit: isardSAT).

4.2.2 Beam angles

4.2.2.1 Purpose and scope

This algorithm computes, for every burst, the angles between the satellite velocity vector and the directions defined by the satellite location and the computed surface locations under the satellite's boresight. The block diagram of this processing algorithm is sketched in Figure 4.2-5.

4.2.2.2 Mathematical description

The algorithm calculates the angles between each satellite velocity vector and the vector connecting every surface location that is "observed" by the satellite at the current satellite burst position and the location itself. These angles are then used by the Azimuth Processing algorithm to steer the beams to the desired surface locations.

The process starts by iterating through the bursts. Then, for each burst, a few steps are followed:

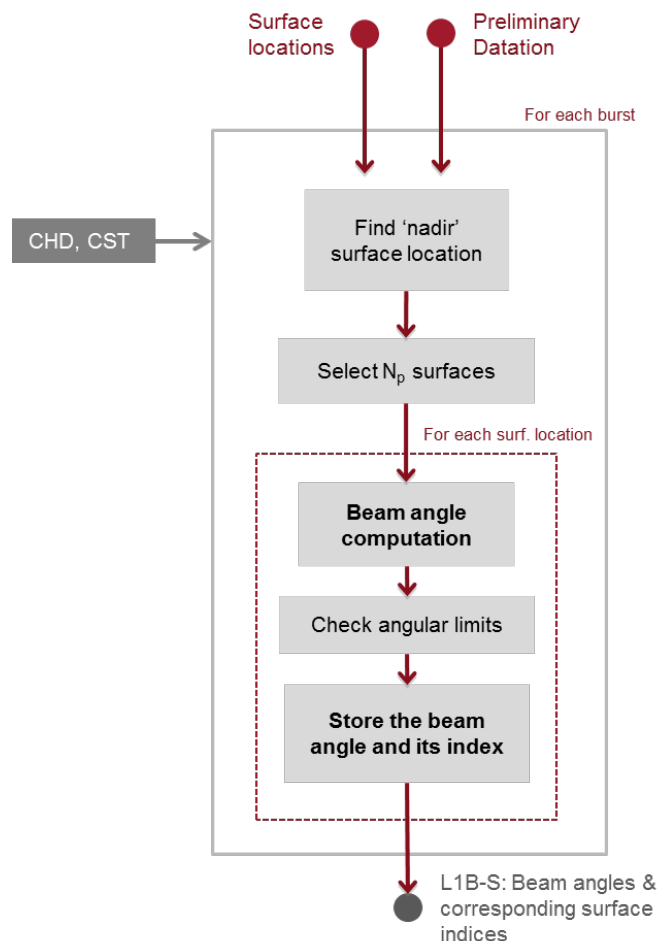


Figure 4.2-5 Flow chart of the beam angles algorithm(credit: isardSAT). CHD and CST refer to the characterization and constants files (see section 4.4).

- Find the surface location closest to the nadir direction and store its index.

- Select N_p surface locations (N_p being the number of pulses per burst): $N_p/2$ forward and $\frac{N_p}{2}$ backwards, (see Figure 4.2-6).
- Finally, store the number of selected surface locations and their indices. These indices will be used later to perform the stack.

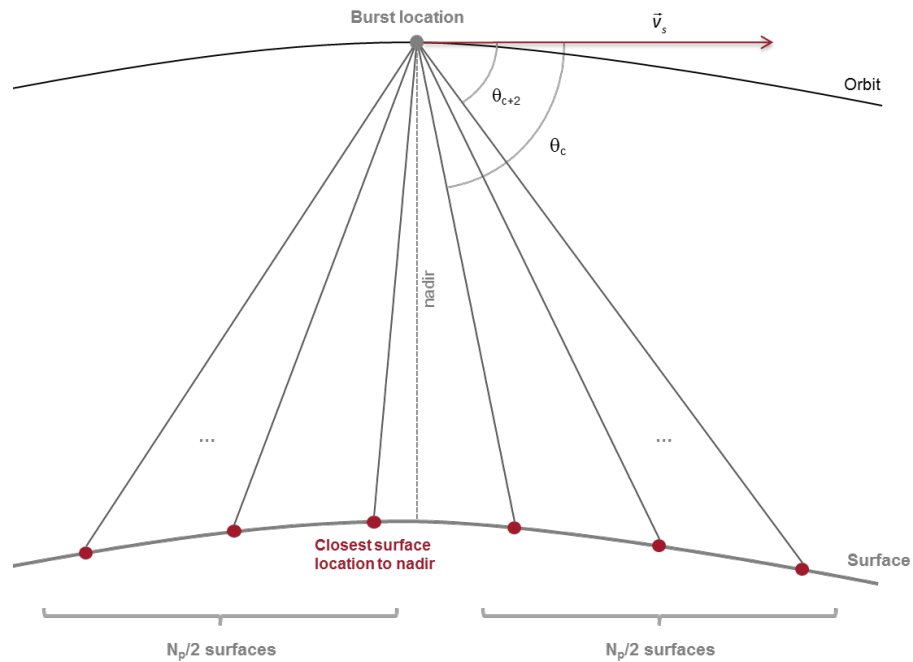


Figure 4.2-6 Geometry of the Beam Angles algorithm (credit: isardSAT). θ_c refers to the beam angle between the satellite velocity's vector and the surface vector from the satellite's position to the specific surface location.

Then, for each surface location the following processing steps are applied:

- Compute the angle between the satellite velocity vector and the satellite to surface direction. This angle is named beam angle:

$$\theta_c = \arccos\left(\frac{\vec{v}_s \cdot \vec{w}_{sat \rightarrow surf}}{|\vec{v}_s| \cdot |\vec{w}_{sat \rightarrow surf}|}\right) \quad \text{Eq. 4.2-3}$$

computed as the dot product or scalar product between the satellite's velocity vector $|\vec{v}_s|$ and the vector from the burst satellite's position to the specific surface location $|\vec{w}_{sat \rightarrow surf}|$. Note that the angular Doppler resolution defined by the angle θ , as shown in Figure 4.2-3 and Figure 4.2-4, corresponds to the angle from nadir direction to the surface direction vector; whereas, the beam angles θ_c , here considered and shown in Figure 4.2-6, are defined between the satellite's velocity vector and the surface direction vector.

Surface focusing

As an optional configuration, specific geographical locations, towards which the beam steering or focusing (over the satellite's track) should be performed, can be input to the Level-1B processor. This is a very interesting approach when operating in coastal regions and it can be also exploited for

colocation with other type of data as RDSAR or LRM. In this case, the location of the closest surface locations (to the given desired geographical locations) are accordingly updated over the track of the satellite as:

1. Transformation from geographical (geodetic) coordinates to Cartesian coordinates over an Earth-Centred Earth-Fixed (ECEF) system.

$$[lon_{int}, lat_{int}, alt_{int}] \rightarrow [x_{int}, y_{int}, z_{int}] \quad \text{Eq. 4.2-4}$$

2. Identification of the surface with the minimum distance to the input desired position (minimum norm over the set of difference vectors)

$$i_{surf}^{min} = i_{surf}, \quad \min \|[x_{int}, y_{int}, z_{int}] - [x(i_{surf}), y(i_{surf}), z(i_{surf})]\| \quad \text{Eq. 4.2-5}$$

3. Projection of the desired location over the satellite's track (projection of the vector joining the previous surface to the one with minimum distance)
4. Updating the surface closest to the desired geographical location

4.2.3 Azimuth processing and stacking

4.2.3.1 Purpose and scope

The purposes of the azimuth processing and stacking algorithm are to steer the beams to the different surface locations and to generate the stacks. The flow chart of the steps corresponding to azimuth processing and stacking is shown in Figure 4.2-7, assuming the exact method for the azimuth processing is used. In this case, there is an additional loop running over each surface when compared to the approximate method.

4.2.3.2 Mathematical description

Azimuth processing:

In order to create Doppler beams, a specific process has to be performed in the along-track direction. This process consists in applying a different phase value $\theta_{beam}(b, p)$ (as defined in Eq 4.2-6 to the different pulses in order to steer the beams towards the surface locations computed in Section 4.2., as originally proposed by Raney (1998)

In order to do so, and as an improvement processing option in this baseline, two different approaches are considered: the exact method (Figure 4.2-8), and the approximate one (Figure 4.2-9), which is an simplification of the former one.

The exact method uses all the beam angles computed in Section 4.2.2 to steer the beams to the surfaces. This implies that there will be an FFT process for each one of the surface locations. On the other hand, the approximate method simply uses the beam angle that is closer to the nadir to spread the other beams and steer them to the other surfaces. This means that the approximate method only goes through one FFT process.

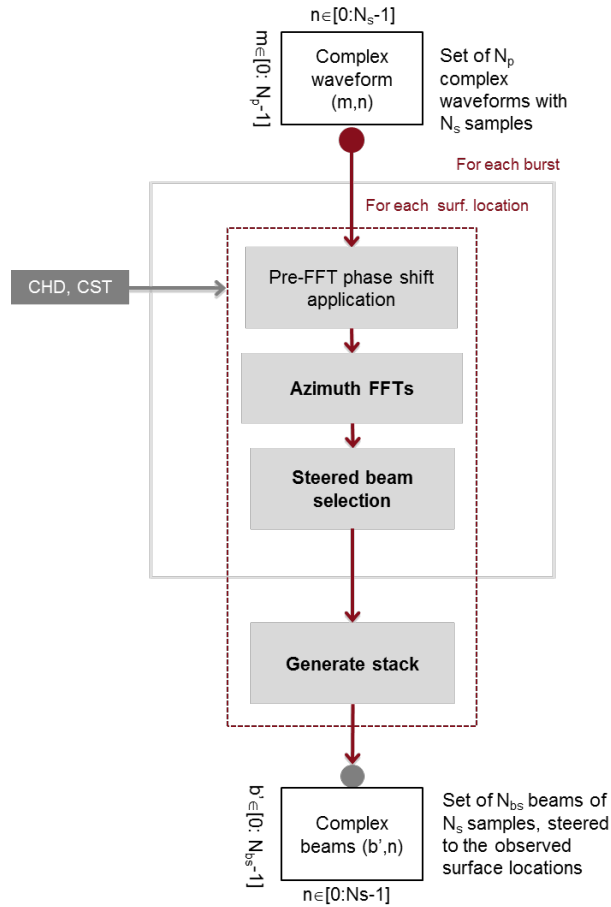


Figure 4.2-7 Block diagram of the azimuth processing and stacking algorithm, considering the exact method (credit: isardSAT). CHD and CST refer to the characterization and constants files (see section 4.4).

Note that the FFT processes come from the angles (or phases) that are applied to the pulses, $\theta_{beam}(b, p)$. These angles have two components:

$$\theta_{beam}(b, p) = \theta_c(b) + \delta\theta(p) = \theta_c(b) + \arcsin\left(\frac{\lambda \cdot p}{2|\vec{v}_s| \cdot N_p \cdot PRI}\right) [rad] \quad \text{Eq. 4.2-6}$$

being b the beam index within a burst $b \in [0, N_b - 1]$; p the pulse index $p \in \left[-\frac{N_p}{2}, \frac{N_p}{2} - 1\right]$; $\theta_c(b)$ the beam angles computed in section 4.2.2; and $\delta\theta(p)$ is the variable part, which leads intrinsically to the FFT in the along-track (or azimuth) dimension. This second part of $\theta_{beam}(b, p)$ is the one that spreads all the beams along the surface locations, being the azimuth angular beam resolution.

From the mathematical point of view, the beamforming operation can be expressed as follows:

$$\Psi_b(k, n) = \frac{1}{\sqrt{N_p}} \cdot \sum_{p=0}^{N_p-1} \Psi_w(p, n) \cdot e^{-2j \cdot \left(\frac{2\pi}{\lambda} \cdot PRI \cdot |\vec{v}_s| \cdot \cos(\theta_c(b)) + \frac{\pi \cdot k}{N_p} \right) \cdot p} \quad \text{Eq. 4.2-7}$$

where k refers to the indexation at beam level. The phase shift applied over the burst $\Psi_w(p, n)$ (weighted in azimuth by a specific window) is hence performing the specific beamforming to the surface of interest. A normalization by number of pulses has been performed to ensure energy is kept constant between domains, pulse and Doppler/beam domains, so Parseval theorem applies. This equation defines the general case of implementing the exact method, so each beam is steered based on the corresponding $\theta_c(b)$, keeping only the central beam for each FFT; while the approximate method exploits the same formulation but a single FFT is performed with the angle closer to nadir, so all the other beams are accordingly steered.

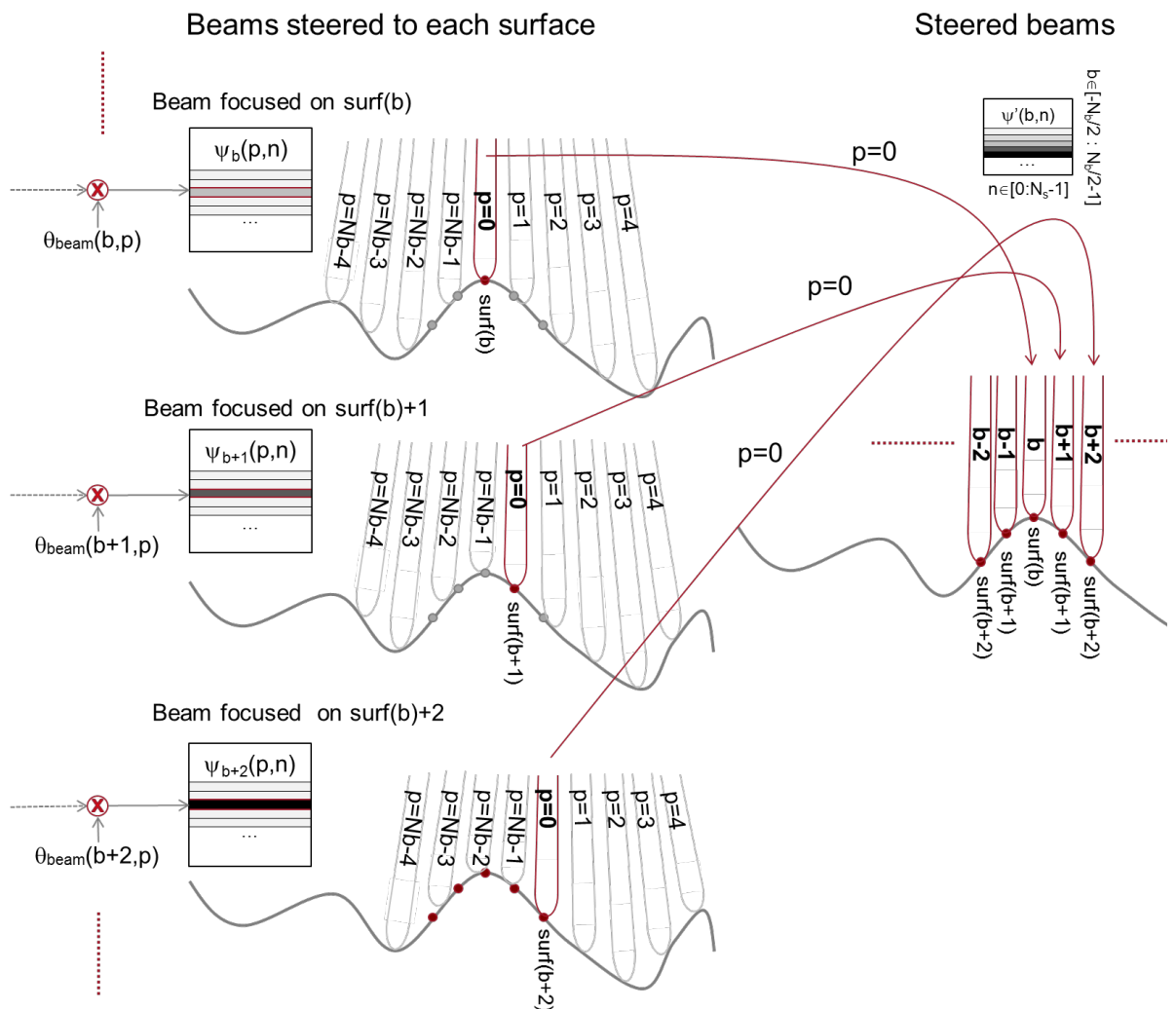


Figure 4.2-8 Exact beam-forming (or steering) geometry; each branch represents the process of focusing the central beam to a specific surface: $\theta_{beam}(b, p)$ refers to the phase used to steer the beams to the specific surface locations (b and p being the beam and pulse indexes, respectively); $\Psi_b(p, n)$ [n corresponds to the sample index] and $\psi'(b, n)$ refer to the set of waveforms before and after the beam steering, respectively (credit: isardSAT)

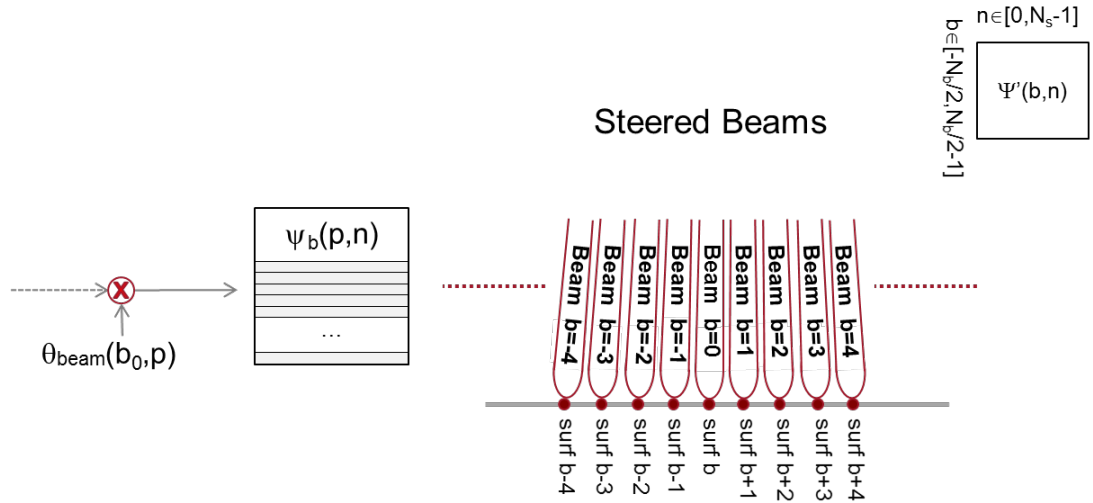


Figure 4.2-9 Approximate beam-forming (steering) geometry (credit: isardSAT). Only the central beam angle b_0 is used and the other beams are equally spaced.

We should note that a specific weighting or window $W(p)$ (Hamming or Hanning) can be optionally included (defined in the configuration file) at burst level before the beam forming procedure (phase ramp + along-track FFT) takes place:

$$\Psi_w(p, n) = \Psi(p, n) \cdot W(p), p \in [0, N_p - 1], n \in [0, N_s - 1] \quad \text{Eq. 4.2-8}$$

where $\Psi(p, n)$ refers to the complex-valued signal in the azimuth time and range-time domains (p and n being the pulse and sample index, respectively).

Such weighting can be used to minimize the impact of side-lobe effects in the Doppler/azimuth PTR (Point Target Response) and, so, the related Doppler ambiguities at the edges of the spectrum (edge beams). This is especially important when operating close to the coast as high reflectivity land scattering can contaminate the signal of interest. We must take into account that this weighting leads to a degradation on the along-track resolution or footprint.

Stack generation:

The stacking consists of regrouping the beams that have illuminated each surface location. This means going from the satellite to the surface point of view as schematically represented in Figure 4.2-10. For each surface all the beams (from the different bursts) pointing to that surface are grouped into a single stack.³

³ It must be noted that the objective of the azimuth processing is to steer for each burst the N_p pulses (which lead to N_p beams steered to different locations on the earth) and so this ends up in the so called 'b' index, relating to the different beams pointing to a specific surface; while the index j in section 4.2.1.2 refers to the sweeping of the different projections of the burst locations on ground and it is used to look for the intersection to generate the new surface location. The index 'l' in Figure 4.2-10 sweeps the total number of surfaces (computed in the surface locations algorithm section 4.2.1) over the track being processed, and so for each one of these locations the stacking is in charge of grouping the focused/steered beams from the different bursts (selecting the proper burst and the proper beam 'b' of that burst).

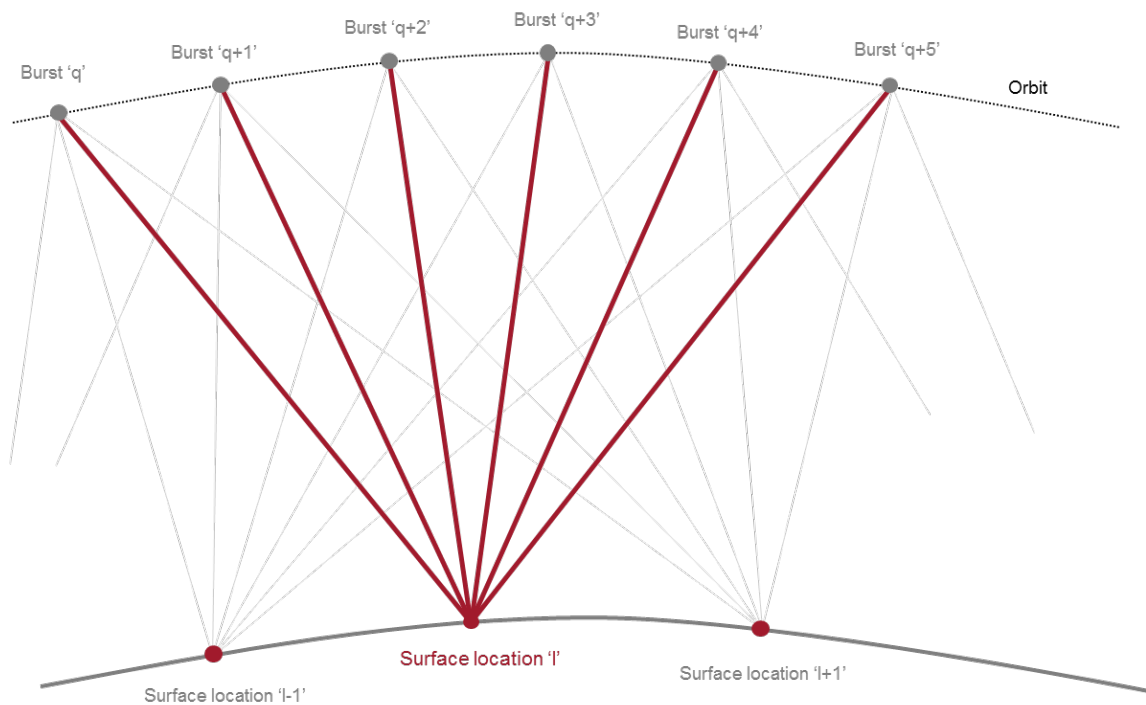


Figure 4.2-10 Stack formation for surface location 'l'. Red lines represent beams illuminating the surface location 'l', hence, the stack. Grey lines are other beams that have been steered to other surface locations (credit: isardSAT).

4.2.4 Geometry corrections

4.2.4.1 Purpose and scope

This algorithm computes and applies all the corrections associated with the geometry of the scenario. These are the Doppler, slant range and window delay misalignments corrections. As the stack has already been generated, these compensations are performed for each stack. In the case of the window delay misalignment, we can apply different methods depending on the observed or desired surface.

The block diagram of this processing algorithm is sketched in Figure 4.2-11.

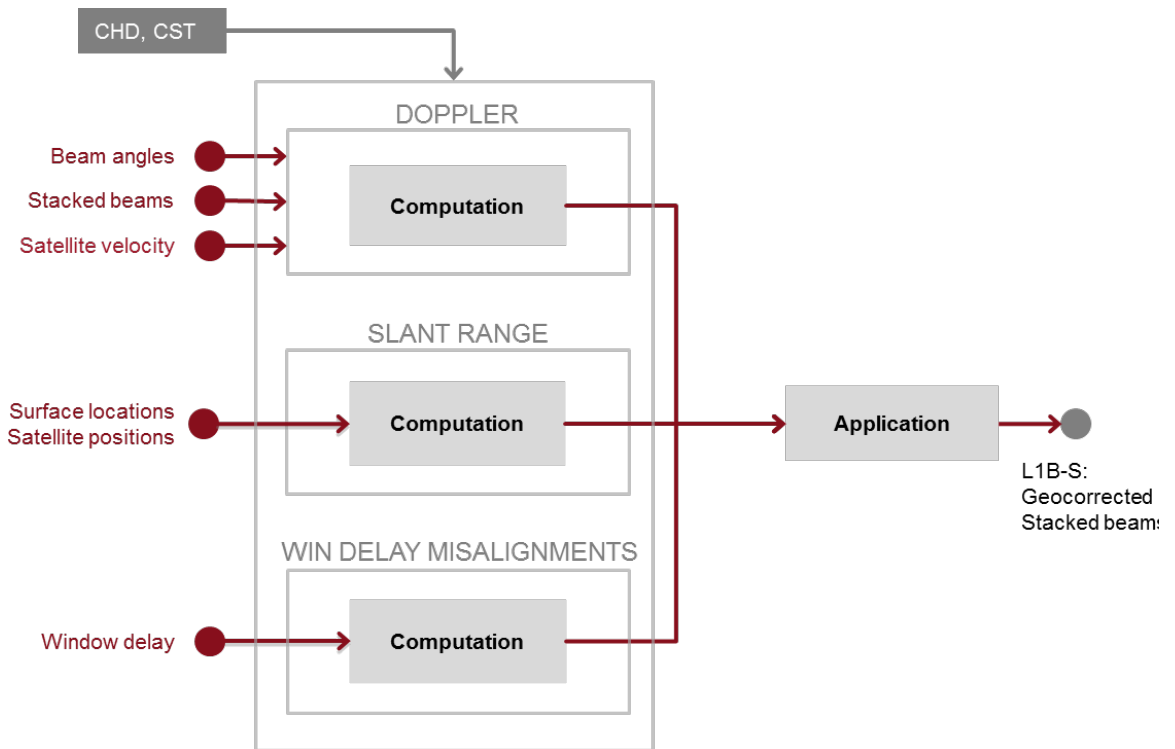


Figure 4.2-11 Block diagram of the geometry corrections algorithm (credit: isardSAT). CHD and CST refer to the characterization and constants files (see section 4.4).

4.2.4.2 Mathematical description

Doppler Correction

The Doppler correction is needed to remove the echoes' frequency shifts due to the sensor-target velocity (compensate for the Doppler offset induced by movement of the platform while transmitting/receiving the pulse, see Prats-Iraola et al. (2014)). The correction is applied to the echoes in time domain, before the FFT step of the range compression.

The frequency shift for a given Doppler direction, in meters, is computed as⁴ (see Figure 4.2-12):

$$\Delta r_D(b') = \underbrace{\frac{c}{2} \cdot \left[\underbrace{\frac{\tau}{B} \cdot \left(-\frac{2}{\lambda} |\vec{v}_s(b')| \cos \theta_c(b') \right)}_{\text{range-delay}} \right]}_{\text{range-shift}} [m], b' \in [0, N_{bs} - 1] \quad \text{Eq. 4.2-9}$$

where $|\vec{v}_s(b')|$ refers to the modulus of the satellite's velocity at the corresponding beam (burst) position, c to the speed of light, τ to the pulse duration, B to the transmitted bandwidth and N_{bs} to the number of beams pointing to that specific surface.

⁴ The physics behind this correction and its derivation are clearly stated in the work of Prats-Iraola et al. 2014. The movement of the platform during transmission/reception produces a net Doppler centroid, which translates into a shift in the range-time. Such Doppler centroid can be computed from the instantaneous Doppler frequency for each beam/burst pointing to that surface, which in turn is converted to range delay through the normalization by the chirp rate and then to delay.

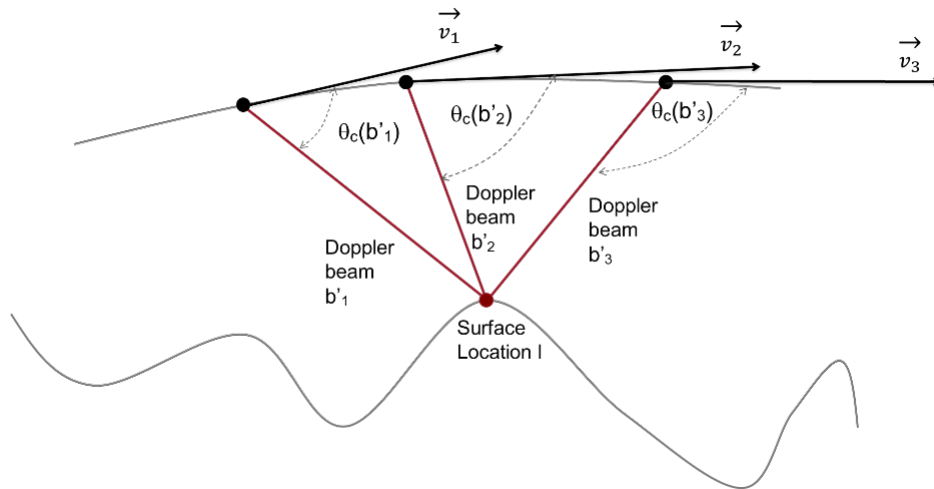


Figure 4.2-12 Geometry of Doppler shift effect (credit: isardSAT). $\theta_c(b')$ refers to the beam angle for each beam/burst focused to that surface; \vec{v} is the satellite velocity vector.

Slant range correction

This correction compensates the range migration produced by the motion of the sensor along the orbit with respect to each surface location. In Figure 4.2-13, the ranges of the surface location 'l', $|\vec{r}(b')|$ are different from the real height $|\vec{h}(l)|$. This difference $\Delta r(b')$ can be computed in range as:

$$\Delta r(b') = |\vec{r}(b')| - |\vec{h}(l)| \quad [m] \quad \text{Eq. 4.2-10}$$

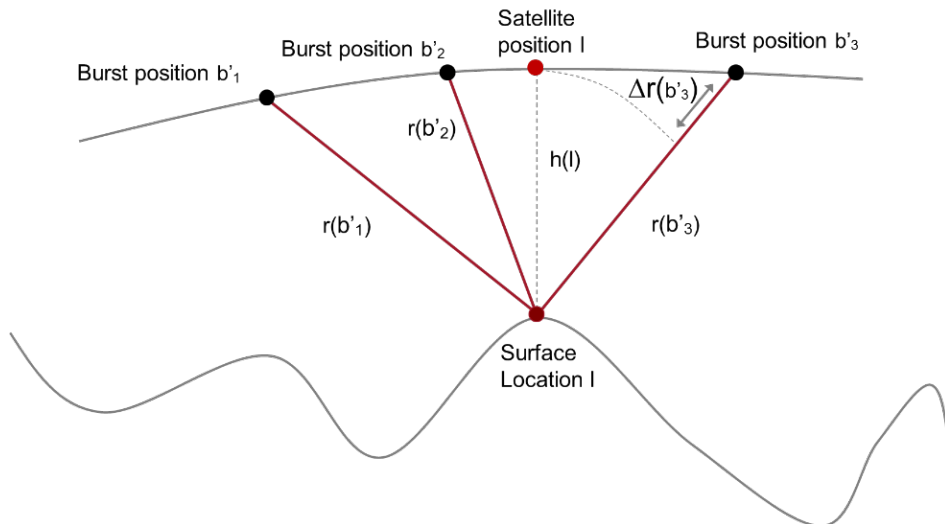


Figure 4.2-13 Geometry of the slant range correction (credit: isardSAT). $r(b')$ refers to the range to the surface location for each beam pointed to that surface and $h(l)$ to the real surface height.

Window delay misalignments

The beams of each stack come from different bursts, with different window delays. These misalignments have to be corrected. In order to do it, the window delay associated with the surface

(and computed in Section 4.2.1) is taken as a reference and the differences with all the window delays of the bursts that have built the stack are computed:

$$\Delta s_{wd}(b') = \frac{\tau_{wdref} - \tau_{wd}(b')}{T_0} [\text{samples}] \quad \text{Eq. 4.2-11}$$

With τ_{wdref} being the reference window delay within the stack (closest approach or with higher power return), $\tau_{wd}(b')$ the window delay associated with the b' beam and T_0 the clock period.

In the case of being on coastal areas, the window delay taken as reference can be chosen as the one of the first ocean surface ahead, rather than the one associated to burst right above the surface that it is still tagged as land. In this way, we ensure that the alignment of the beams of the stack is done such that the ocean waveform is recovered (and not the one over land). Results achieved by using this approach are discussed in (Garcia P., 2018)

All these three corrections, not being an integer number of samples, are applied as a frequency shift by multiplying the beam waveforms in time by an exponential (Cumming and Wong, 2005; Raney, 1998):

$$\exp \left\{ j \frac{2\pi}{N_s} \cdot \Delta s(b') \cdot n \right\} \quad \text{Eq. 4.2-12}$$

where $\Delta s(b')$ corresponds to the total correction in samples (N_s being the total number of range samples).

Finally, the window delay associated with each surface location has to be replaced by the reference window delay within the stack.

4.2.5 Range compression

4.2.5.1 Purpose and scope

This algorithm performs the range compression of the input bursts and then generates the power waveforms. The block diagram of this processing algorithm is sketched in Figure 4.2-14.

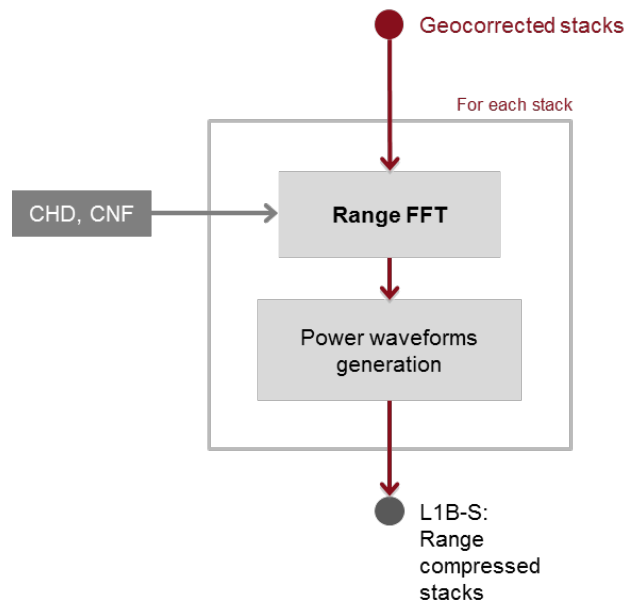


Figure 4.2-14 Block diagram of the range compression algorithm (credit: isardSAT). CHD and CNF refer to the characterization and configuration files, respectively, see section 4.4

4.2.5.2 Mathematical description

The time domain waveforms are converted into beams (frequency domain) by use of a Fast Fourier Transform (FFT).

The on-board pulse compression used commonly in radar altimeters samples the radar echo at a frequency equal to the pulse bandwidth, which for the power echo results in an undersampling factor of 2 as described in Jensen (1999) and Smith & Scharroo (2014). A simple zero-padding (on the complex signal) before performing the FFT, can alleviate the related aliasing. In this way a better sampling of the power waveform leading edge is obtained, especially important for low SWH or very specular echoes (e.g., leads or sea ice), in a way that both the range and SWH estimations are improved as stated in Smith and Scharroo (2014) for CryoSat-2 data.

We should note, as pointed out in Smith and Scharroo work (2014), that zero-padding can provide improved retrievals simply because more samples are available for the geophysical fitting of the model. This means that the leading edge can be properly sampled (this is especially interesting for very specular returns with low SWH) and that more samples can be available to perform a better estimation of the noise floor to be included in the retracking model. In this line, and for very small SWH, the resolution of the instrument (defined by the transmitted bandwidth) is not able to discriminate the leading edge, and so the inclusion or not of zero-padding will not help at all. On the other hand, and for high SWH, the inclusion of zero-padding does not provide any additional improvement, as the contribution of the power waveform spectrum outside the Nyquist bandwidth criterion is very low (differently from Jensen's claim, which ensures that deramped altimetric power waveforms are inevitably aliased). Therefore, and contrary to what is stated in Jensen (1999), zero-padding does not need to be necessarily applied regardless of the type of scenario being imaged (as it comes out from the analysis of the work of Smith and Scharroo 2014).

A zero-padding can be optionally considered in the time-domain, such that after FFT operation, an interpolated version of the range-compressed signal is obtained (Cumming and Wong, 2005). The impact of this operation is a finer range step (higher sampling frequency). Note that this process increases the number of samples of the output variable. After that, the power waveforms are computed (detection step):

$$\Psi_{\text{stack}}(b', n') = \left| \text{FFT}_{zp}(\psi_{gm_stack}(b', n)) \right|^2, b' \in [0, N_{bs} - 1], n' \in [0, N_s \cdot ZP - 1], n \in [0, N_s - 1] \quad \text{Eq. 4.2-13}$$

where $\psi_{gm_stack}(b', n)$ corresponds to the stack after applying the geometry corrections and ZP refers to the zero-padding factor or oversampling factor used in the range-compression via FFT.

Moreover, since the geometry corrections have been applied through an exponential (that is equivalent to a circular shift in the other domain as finite-length signals are considered), some samples may have suffered a wrapping. This has to be solved through a mask and force these samples to zero. This mask is computed through the sum of all the three geometry corrections together and it is applied the following way:

$$\Psi'_{\text{stack}}(b', n') = \Psi_{\text{stack}}(b', n') \cdot H_{\text{mask}}(b', n'), b' \in [0, N_{bs} - 1], n' \in [0, N_s \cdot ZP - 1] \quad \text{Eq. 4.2-14}$$

4.2.6 Multi-looking

4.2.6.1 Purpose and scope

The objective of this algorithm is performing an average (incoherent integration) of all the waveforms that form each stack.

4.2.6.2 Mathematical description

The steps to multi-look the echoes in a stack, into a single waveform, are described in the following lines. Each step corresponds to each stage in the block diagram of Figure 4.2-15.

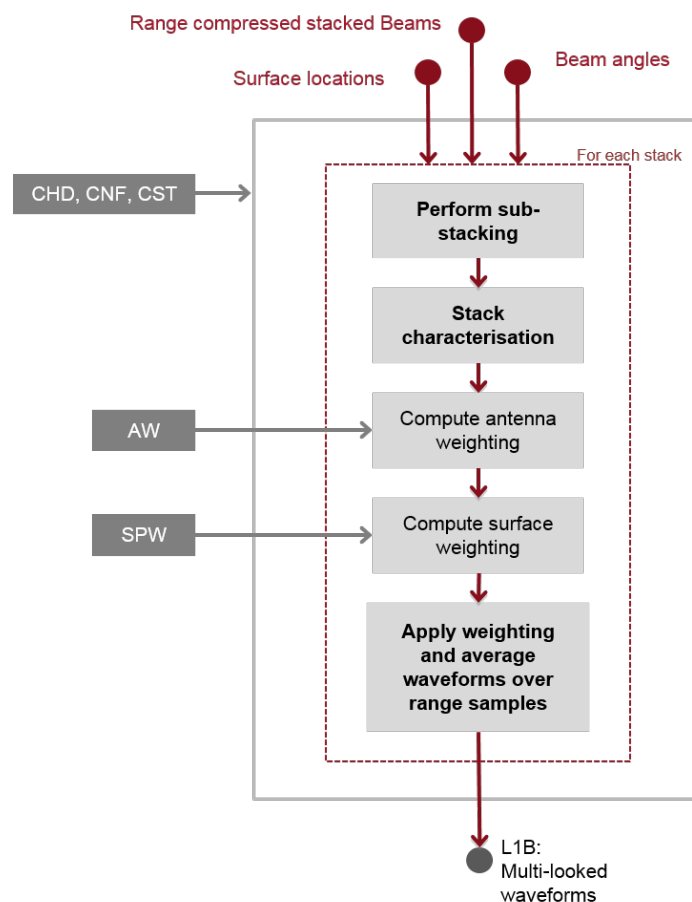


Figure 4.2-15 Block diagram of the multi-looking algorithm (credit: isardSAT). CHD, CNF and CST refer to the characterization, configuration and constants files, respectively; and AW and SPW are the antenna and surface weighting files (see section 4.4).

For each stack, a few steps must be followed:

- **Sub-stacking:** In order to compute the stack characteristic parameters (3 dB width, skewness and kurtosis of a Gaussian power waveform fitting), a sub-stacking is performed. This means grouping the total power of the beams in small groups so as to reduce the noise.
- **Retrieve stack characteristics:** This reduction of the noise, leads the Gaussian fitting to a better performance, and then the related 3 dB width, skewness and kurtosis are retrieved.
- **Antenna weightings computation:** Before averaging the stacks, it might be of interest to remove or compensate for the antenna weighting (different beams are differently affected by the antenna

pattern). These weightings, which are optionally activated (in the configuration file), can be both pre-set and/or provided by the user.

- Antenna weighting and averaging: After that, the weighting(s) are optionally applied and the waveforms are averaged over range samples:

$$\bar{\Psi}_{stack}(n') = \frac{1}{\sum_{b'=0}^{N_{bs}-1} W(b')} \cdot \sum_{b'=0}^{N_{bs}-1} W(b') \cdot \Psi'_{stack}(b', n'), \quad \text{option } \Psi'_{stack}(b', n') \neq 0 \quad \text{Eq. 4.2-15}$$

This operation (depending on a configuration flag) can be done taking into account all the samples or only the non-zero ones ($\Psi'_{stack}(b', n') \neq 0$). Typically, all the range samples (even the zero-valued ones) are used when multi-looking the stack, which reduces the mean power on those samples, producing a distortion of the waveform. This is an issue of present discussion and so the re-trackers should be accordingly implemented taking into account the effect of such mask.

The Doppler- or beam-dependent weighting optionally included in the processing baseline may lead to an improved SNR, and hence to an improved SWH retrieval.

4.2.7 Sigma0 scaling factor

4.2.7.1 Purpose and scope

This algorithm is in charge of computing the scaling factor that allows to convert the power of the multi-looked waveform into σ^0 values (normalized radar cross section values). The flow chart of this algorithm is shown in Figure 4.2-16.

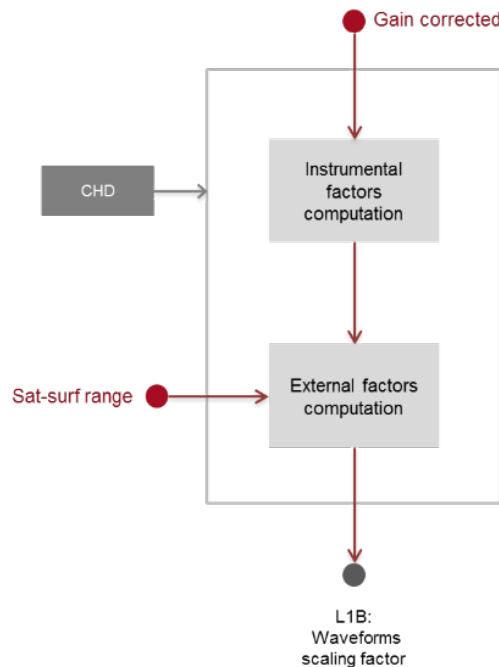


Figure 4.2-16 Block diagram of the sigma0 scaling factor algorithm (credit: isardSAT). CHD refers to the characterization file (see section 4.4).

4.2.7.2 Mathematical description

Based on the classical radar equation of the received power (Curlander and McDonough, 1991), the scaling factor per each beam pointing a specific surface can be obtained as:

$$k_{\sigma}(b') = \frac{4\pi}{P_{TX} \cdot G_0^2 \cdot \lambda^2} \cdot \frac{(4\pi \cdot r^2(b'))^2}{A_{surf}(b')}, [W^{-1}] \quad \text{Eq. 4.2-16}$$

where the first fractional term is the so called *instrumental scaling factor* and the second one represents the *external effects*.

P_{TX} is the transmitted average power; G_0 refers to the antenna gain at boresight (assuming the beam-dependent antenna pattern impact is compensated for in the antenna weighting step of the multi-looking algorithm Section 4.2.6 or in the retracking model); $r(b')$ is the slant range distance for the specific beam pointing the surface and $A_{surf}(b')$ corresponds to the on-ground and beam-dependent, resolved surface area.

The user can optionally provide the normalized sigma0 along-track pattern (as a function of the look angle) to obtain the scaling factor per beam.

Then, the sigma0 scaling factor to be applied over the multi-looked power waveform is obtained as the average value over the different beam-dependent scaling factors:

$$k_{\sigma^0} = \frac{1}{N_{bs}} \sum_{b'=0}^{N_{bs}-1} k_{\sigma^0}(b'), \quad [W] \quad \text{Eq. 4.2-17}$$

4.3 Development choices and trade offs

A set of new algorithms is being considered in the implemented Level 1-B processing as already described within the different processing steps in Section 4.2. The new processing stages, which might potentially improve the performance, can be summarized as:

- Burst azimuth weighting
- Azimuth processing method: exact or approximate
- Surface focusing
- Antenna weighting
- Multi-looking with zeroes method
- Zero-padding in across-track (range oversampling factor)
- New sigma-0 computation method

4.4 Data flow

For details on the input/output description of the products and the format specification of the output products for the Delay-Doppler SCOOP processor please refer to SCOOP deliverables D2.1 IODD and D2.3 PSD.

4.4.1 Input data

The input data for the SCOOP Delay-Doppler processor consist of L1A calibrated data for Sentinel-3 and of calibrated FBR CryoSat-2 baseline-C products⁵.

4.4.2 Ancillary information

The ancillary data can include apart from the auxiliary files (static and dynamic) additional information such as DEM, in-situ measurements from buoys, radiometers, and so on.

- **Static auxiliary files:**
 - **Characterisation file (CHD):** includes system on-ground characterization (general, time pattern, platform, antenna, calibration...)
 - **Configuration file (CNF):** Contains all the Delay-Doppler or SAR processor switches and processing options that can be accordingly activated/deactivated.
 - **Constants File (CST):** includes the main physical constants used in the Level-1A to Level-1B processor.
 - Characterization arrays⁶:
 - **CAL2** masks corrections
 - **CAL1** intraburst corrections
 - **Antenna weighting file (AW):** includes the antenna pattern as a function of the antenna pointing angle, which is compensated before the multi-looking takes place.
 - Delay-Doppler **processor weighting** files:
 - **Azimuth weighting file:** includes the weighting applied at burst level prior to azimuth processing.
 - **Surface weighting file (SPW):** includes the specific weighting for a given surface model as a function of look angle (applied before multi-looking).
- **Dynamic auxiliary files:**
 - **Orbit files:** include predicted orbit file, DORIS preliminary/precise orbit files, DORIS navigator file, GNSS orbit file.
 - **Attitude files:** include attitude restituted file, star tracker L0 files, star tracker configuration file, AOCS attitude file.
 - **USO drift file:** includes measured drift of the USO from its nominal clock value.
 - **CoM file:** includes variations on the satellite's centre of mass during the mission.
- **Land-sea mask (or water body mask file)**

4.4.3 Output

The science output files of the Delay-Doppler processor are: Level-1B-S (L1B-S) and L1B:

⁵ Calibration values are reported in the document "CryoSat characterisation for FBR users" available at <https://wiki.services.eoportal.org/tiki-index.php?page=CryoSat+Technical+Notes>.

⁶ CAL2 mask corrections and CAL1 intraburst corrections are required to calibrate the FBR baseline-C from CryoSat-2.

- **L1B-S** is an intermediate and optional output product of the SAR processor. It contains fully SAR-processed and calibrated SAR complex echoes arranged in stacks for each surface after slant range correction and before the multi-looking takes place.
- **L1B** is the final science product at the output of the SAR processor. It contains geo-located and fully calibrated multi-looked SAR power echoes.

5 Algorithm description: Echo modelling / retracking

Note: isardSAT took on responsibility for L1B to L2 SAR processing (echo modelling/retracking) for the second phase of the SCOOP project. Their processing approach is described in a separate ATBD (Makhoul, 2019)

5.1 Theoretical description, physics of the problem

The main objective of the retracker is to estimate the Level-2 geophysical parameters (i.e., sea surface height (SSH), significant wave height (SWH), and backscatter coefficient (*denoted as σ_o*)). The way to proceed is by fitting a simulated SAR waveform, with the real SAR waveform provided by the L1b data. Using a mean square minimization error approach, the SSH, SWH, and σ_o can be estimated by finding the solution that minimizes the mean square error (MSE), between the real SAR waveform and the simulated one. The MSE approach used for CryoSat-2 and proposed for Sentinel-3 is based on a Levenberg Marquardt optimization algorithm (Marquardt et al., 1963), which is a combination of the steepest-descent optimization method (Lambers et al., 2011-12) and the Newton Method (Ortega et al., 1970). Therefore, one of the critical points is to define the SAR Waveform.

In SAR altimetry, the echo over the ocean can be expressed as the convolution of the surface impulse response (P_{surf}), the system point target response (PTR), and the sea surface height probability density function (PDF_{sea}).

$$P(f, t) \propto \sigma_o G^2(f, t) P_{surf}(f, t) * PTR(f, t) * PDF_{sea} \quad \text{Eq. 5.1-1}$$

where σ_o is the backscatter coefficient, and G is the antenna gain.

Eq. 5.1-1, which depends on geophysical, geometrical, satellite and orbit parameters, can be solved in different ways, e.g., numerically, analytically, or empirically. The numerical approach (Phalippou & Enjolras, 2007, and Boy et al., 2012) provides an exact solution, however is expensive in terms of computation requirements, since the convolution in Eq 5.1.1 has to be computed for a wide range of geophysical, geometrical and orbital parameters. The empirical approach (Sandwell et al. 2011, and Garcia 2014) proposes an empirical fully-analytical model, which provides a simple formulation. This approach is based on three assumptions: (1) only the nadir-looking Doppler beam contributes significantly to the multi-looked waveform, (2) the mispointing of the antenna is small compared to the antenna beamwidth, (3) the half-width of the nadir-looking Doppler beam is very narrow compared to the radius of the pulse-limited circle. However, this approach is found to have difficulty in accurately fitting the 'toe' of the waveform at the onset of the leading edge, and also in estimating very low values of SWH.

The SAMOSA retracker is based on both a semi-analytical approach (SAMOSA-2 (Ray et al. 2013)), and fully analytical approaches (SAMOSA-1 (Martin-Puig et al., 2008) and SAMOSA-3 (Gommenginger et al., 2012)). SAMOSA-2 is the approach that provides the most complete solution, accounting for the curvature effect along and across track, the ellipticity of the antenna pattern, non-Gaussian ocean surface statistics, radial velocity and mispointing effects. However, compared with the analytical approaches, this approach is more demanding in terms of computation requirements.

SAMOSA-3 is a simplification of the SAMOSA-2, where the basis functions are implemented without numerical integrations for large values of the input parameter (lookup tables are used instead), and the altimeter waveform model is truncated in an analytical expression. These simplifications result in a reduced averaged time to retrack each waveform, with a similar performance to SAMOSA-2, i.e.

small biases in the estimation of the epoch (range bin difference is lower than 0.1), and almost identical SWH.

For Sentinel-3, the approach proposed is based on the SAMOSA waveform model, as described in [Ray et al., 2014], with the different updates done within the CryoSat Plus for Ocean (CP4O) project, i.e. appropriate handling of the energy distribution over the echoes of the Delay-Doppler stack, computation of the Point Target Response (PTR) as stated in the S3 IPF, an appropriate estimation, and a complete implementation of the SAMOSA-2 model. In this context, different implementations for the retracker will be available (e.g. complete implementation of the SAMOSA-2 model analytically, using LUTS, or the SAMOSA-3 truncated model).

5.2 Algorithm definition: processing steps and mathematical description

This section deals with the algorithm definition to develop the SAR waveforms, describing the main terms showed in Eq. 5.1-1, and including its mathematical description. In this section the following points are recalled from works done in the framework of SAMOSA-3 along with the associated mathematical formulation (Gommenginger et al, 2012), and (Ray and Martin-Puig, 2012). Topics covered are:

- Observation scenario.
- EM scattering Model.
- Antenna Gain.
- Sea Height distribution.
- Waveform Expression.

5.2.1 Geometry Scenario

The geometry is based on the Elliptical surface (WGS84), with a semi-major axis of earth (denoted as a) equal to 6378137m, and semi-minor axis of earth (b) equal to 6356752.3142m. Additionally the geometry can be expressed in Cartesian coordinates (x, y, z) as

$$\begin{aligned} x &= a \cos \theta_{plat} \cos \phi_{plon} \\ y &= a \cos \theta_{plat} \sin \phi_{plon} \\ z &= b \sin \theta_{plat} \end{aligned} \quad \text{Eq. 5.2-1}$$

where θ_{plat} corresponds to the planetographic latitude and ϕ_{plon} is the planetographic longitude. Figure 5.2-1 shows the observation geometry with and without mis-pointing.

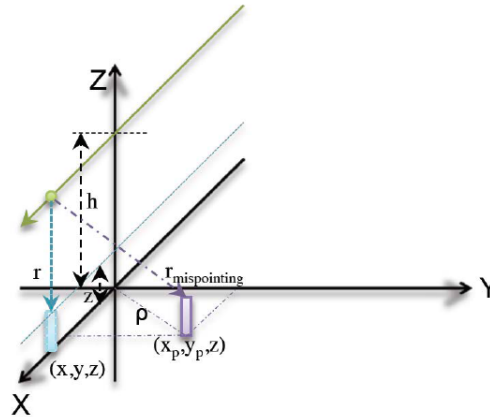


Figure 5-1 Observation geometry with and without mis-pointing (credit: NOC).

Scattering points on the surface, can be referenced by a 2D vector $\vec{\rho}$, which modulus is equal to $\vec{\rho}^2 = x^2 + y^2$. From it, the distance from the satellite to the scatter can be written as,

$$r = h - z + \frac{\alpha}{2h} \rho^2 + \vartheta[1mm] \quad \text{Eq. 5.2-2}$$

where h is the spacecraft altitude and z is the height of the scatterer, and α is the Earth curvature effect given by,

$$\alpha = 1 + \frac{h}{R_e}, \quad \text{Eq. 5.2-3}$$

R_e is the Earth radius, defined as a function of the geodetic parameters a and b ,

$$R_e = \sqrt{a^2 \cos^2 \theta_{plat} + b^2 \sin^2 \theta_{plat}}, \quad \text{Eq. 5.2-4}$$

The effect of mispointing in this model has been introduced as a pointing displacement on the surface. Therefore, if the antenna is no longer pointing at nadir but different, it will be illuminating towards a position displaced $(x-x_p, y-y_p)$. Where x_p, y_p are the mispointing coordinates, which can be easily related to pitch (θ_{pitch}) and roll (θ_{roll}) angles: $x_p = h \theta_{pitch}$ and $y_p = -h \theta_{roll}$

Note that signs of pitch and roll follow the flight dynamics coordinates system as shown in Figure 5-2

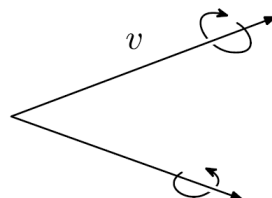


Figure 5-2. Flight dynamics coordinate system assumed for mis-pointing calculation.

5.2.2 EM Scattering Model

According to Valenzuela et al. (1977) and Gommenginger et al., (2012) the EM model has assumed isotropic rough surface of Gaussian statistics. Therefore, the scattering amplitude can be defined as,

$$\sigma(x, y) = \sigma_o(0) \exp(-\alpha_\sigma(x^2 - y^2)), \quad \text{Eq. 5.2-5}$$

With α_σ given by,

$$\alpha_\sigma = \frac{L_c^2}{2\sigma_z^2 h^2} \quad \text{Eq. 5.2-6}$$

Where L_c is the Ocean correlation length, σ_z is the RMS of the specular points in reference to the mean sea level (MSL), and h is the satellite height. Eq. 5.2-5 can be expressed as

$$\sigma(x, y) = \sigma_o(0) \exp\left(-\frac{\tan^2 \theta}{\sigma_{slopes}^2}\right) \quad \text{Eq. 5.2-7}$$

where σ_{slopes}^2 is defined as the variance of the total sea surface slope (i.e., mean square-slopes (MSS)), and θ is the observation angle, with σ_{slopes}^2 defined as,

$$\sigma_{slopes} = \frac{\sqrt{2}\sigma_z}{L_c}. \quad \text{Eq. 5.2-8}$$

and where σ_z is the rms of the height of the specular points, and L_c is the ocean correlation length. From Eq. 5.2-8 and Eq. 5.2-6 it follows that α_σ and σ_{slopes} are related as,

$$\alpha_\sigma = \frac{1}{h^2 \sigma_{slopes}^2}, \quad \text{Eq. 5.2-9}$$

To finish, a parameter v is introduced for convenience, which simply can be defined as the inverse of the MSS,

$$v = \frac{1}{MSS}, \quad \text{Eq. 5.2-10}$$

5.2.3 Antenna Gain

Based on the CryoSat-2 case, the gain of the antenna without mis-pointing can be expressed as (Gommenginger et al., 2012),

$$G(x, y) = G_o \exp\left(-4\ln(2) \frac{x^2}{h^2 \theta_x^2} - 4\ln(2) \frac{y^2}{h^2 \theta_y^2}\right) \quad \text{Eq. 5.2-11}$$

where θ_x is the full along-track width of the beam at the half power point, and θ_y is the equivalent for across-track. Eq. 5.2-11 can be rewritten as a function of α_x , and α_y as ,

$$G(x, y) = G_o \exp\left(-\alpha_x \frac{x^2}{2} - \alpha_y \frac{y^2}{2}\right), \quad \text{Eq. 5.2-12}$$

where α_x , and α_y are given by,

$$\begin{aligned} \alpha_x &= \frac{sh_x 8 \ln(2)}{h^2 \theta_x^2} \\ \alpha_y &= \frac{sh_y 8 \ln(2)}{h^2 \theta_y^2} \end{aligned} \quad \text{Eq. 5.2-13}$$

With sh_x and sh_y being shape factors that take into account any disfunction of the antenna focal point. Note that by default sh_x and sh_y will be set up to 1 (Gommenginger et al., 2012, and Ray et al., 2012)..

If now the impact of the mis-pointing is considered, Eq. 5.2-12 can be rewritten as,

$$G(x, y) = G_o \exp\left(-\alpha_x \frac{(x - x_p)^2}{2} - \alpha_y \frac{(y - y_p)^2}{2}\right), \quad \text{Eq. 5.2-14}$$

where x_p and y_p represent the mis-pointing coordinates, that can be expressed as a function of the pitch (θ_{pitch}), and roll (θ_{roll}) as

$$\begin{aligned} x_p &= h \theta_{pitch} \\ y_p &= -h \theta_{roll} \end{aligned} \quad \text{Eq. 5.2-15}$$

From Eq. 5.2-15 it can be noted that for a positive pitch angle the displacement x_p will be positive and for a positive roll angle the displacement y_p will be negative.

If now is considered that for Sentinel-3 the antenna will be circular and not elliptical (as it was for CryoSat-2), it can be assumed that $\theta_x = \theta_y = \theta_c$, or $\alpha_x = \alpha_y$. Considering this, the antenna gain becomes,

$$G(\theta) \approx G_o \exp\left(-\frac{4 \ln(2)}{\theta_c} \sin^2(\theta)\right) \quad \text{Eq. 5.2-16}$$

5.2.4 Sea height distribution

Based on Rodriguez (1988), the probability density of the sea height can be defined as,

$$p(\eta) = \frac{1}{\sqrt{2\pi}\sigma_z} \left(1 + \frac{\lambda_s}{6}(\eta^3 - 3\eta)\right) e^{-\eta^2/2} \quad \text{Eq. 5.2-17}$$

where η is the sea height relative to the mean sea height and EM bias, scaled for the standard deviation of the sea height. It can be expressed as,

$$\eta = \frac{z_o - \langle z_o \rangle + z_{EM}}{\sigma_z} \quad \text{Eq. 5.2-18}$$

where σ_z is the standard deviation of the sea height, $\langle z_o \rangle$ is the mean sea height, and z_{EM} is the electromagnetic bias.

5.2.5 PTR width

The squared Delay-Doppler PTR in the SAMOSA model can be approximated by a Gaussian function as.

$$PTR = \text{sinc}^2(x) = e^{-\left(\frac{x}{\sqrt{2\alpha_p}}\right)^2} \quad \text{Eq. 5.2-19}$$

where α_p is a scaling factor. Based on the current SAMOSA v2.3 implemented on the S3 IPF α_p , is approximated as 0.3831 for the Azimuth PTR Gaussian approximation, and as a 0.513 for the Range PTR Gaussian approximation.

5.2.6 Waveform Truncated Analytical Expression

This section provides the truncated analytical expression of the waveform implemented in SAMOSA-3 that will be used as a reference for the Sentinel-3 retracker.

The starting point will be the full waveform defined in the SAMOSA CCN project (Ray and Martin-Puig, 2012), as

$$\begin{aligned} P_{k,l} = P_u \sqrt{g_l} \Gamma_{k,l} & \left\{ \left[1 - \frac{\langle z_o \rangle - z_{EM}}{L_\Gamma} T_k(y_p) \right] \left[f_o \left(g_l \left(k + \frac{\langle z_o \rangle - z_{EM}}{L_x} \right) \right) \right. \right. \\ & + \frac{\lambda_s}{2} g_l^3 \sigma_s^3 f_1 \left(g_l \left(k + \frac{\langle z_o \rangle - z_{EM}}{L_x} \right) \right) - \frac{\lambda_s}{6} g_l^3 \sigma_s^3 f_3 \left(g_l \left(k + \frac{\langle z_o \rangle - z_{EM}}{L_x} \right) \right) \Bigg] \\ & - \frac{\sigma_z}{L_\Gamma} T_k(y_p) \left[\frac{\lambda_s}{2} (1 - g_l^2 \sigma_s^2) g_l^2 \sigma_s^2 f_o \left(g_l \left(k + \frac{\langle z_o \rangle - z_{EM}}{L_x} \right) \right) \right. \\ & - g_l \sigma_s f_1 \left(g_l \left(k + \frac{\langle z_o \rangle - z_{EM}}{L_x} \right) \right) \\ & + \frac{\lambda_s}{2} (1 - 2g_l^2 \sigma_s^2) g_l^2 \sigma_s^2 f_2 \left(g_l \left(k + \frac{\langle z_o \rangle - z_{EM}}{L_x} \right) \right) \\ & \left. \left. + \frac{\lambda_s}{6} g_l^4 \sigma_s^4 f_4 \left(g_l \left(k + \frac{\langle z_o \rangle - z_{EM}}{L_x} \right) \right) \right] \right\} \end{aligned} \quad \text{Eq. 5.2-20}$$

Neglecting the skewness, Eq. 5.2-20, is reduced to,

$$\begin{aligned} P_{k,l} = P_u \sqrt{g_l} \Gamma_{k,l} & \left\{ \left[1 - \frac{\langle z_o \rangle - z_{EM}}{L_\Gamma} T_k(y_p) \right] f_o \left(g_l \left(k + \frac{\langle z_o \rangle - z_{EM}}{L_x} \right) \right) \right. \\ & \left. + \frac{\sigma_z}{L_\Gamma} T_k(y_p) g_l \sigma_s f_1 \left(g_l \left(k + \frac{\langle z_o \rangle - z_{EM}}{L_x} \right) \right) \right\} \end{aligned} \quad \text{Eq. 5.2-21}$$

where the subscript k stands for the across-track index (also referred as range gate or range bin), and l for the along-track (Doppler), and P_u is a variable that accounts for all the multiplicative factors.

It can be noted that Eq.5.2-20, is dependent on the function $f_n(\xi)$, and g_l , which can be expressed as,

$$f_n(\xi) = \int_0^\infty e^{-\frac{1}{2}(\xi-u^2)^2} (\xi - u^2)^n du \quad \text{Eq. 5.2-22}$$

$$g_l = \sqrt{\frac{2\alpha_g}{1 + 4\left(\frac{L_x}{L_y}\right)^2 (l - l_s)^2 + 2\alpha_g \left(\frac{\sigma_z}{L_z}\right)}} \quad \text{Eq. 5.2-23}$$

where α_g (Gaussian sinc approximation parameter), L_x (along-track length scale), L_y (across-track length scale), and L_z (height length scale), and l_s (along-track index that contains the specular points) are equal to,

$$\alpha_g = 1.6813 \quad \text{Eq. 5.2-24}$$

$$L_x = \frac{ch}{2V_s f_c T} \approx 293\text{m} \quad \text{Eq. 5.2-25}$$

$$L_y = \sqrt{\frac{ch}{\alpha B_r}} \approx 777\text{m} \quad \text{Eq. 5.2-26}$$

$$L_z = \frac{c}{2B_c} \approx 0.4083\text{m} \quad \text{Eq. 5.2-27}$$

On the other side, $\Gamma_{k,l}$ can be expressed as.

$$\Gamma_{k,l} = \exp\left[-\alpha_y y_p^2 - \alpha_x (x_l - x_p)^2 - \alpha_\sigma x_l^2 - (\alpha_y + \alpha_\sigma) y_k^2\right] \cosh(2\alpha_p y_p y_k) \quad \text{Eq. 5.2-28}$$

Where x_l and y_p are given by,

$$x_l = L_x l \quad \text{Eq. 5.2-29}$$

$$y_k = \begin{cases} L_y \sqrt{k} & \text{if } k > 0 \\ 0 & \text{otherwise} \end{cases} \quad \text{Eq. 5.2-30}$$

From E1. 5.2-28, x_p , and y_p define the location of the centre of the beam on the surface. In addition α_x , α_y , and α_σ are defined as,

$$\alpha_x = \frac{8 \ln(2)}{h^2 \theta_x^2} \quad \text{Eq. 5.2-31}$$

$$\alpha_y = \frac{8 \ln(2)}{h^2 \theta_y^2} \quad \text{Eq. 5.2-32}$$

$$\alpha_\sigma = \frac{L_c^2}{2\sigma_z^2 h^2} \quad \text{Eq. 5.2-33}$$

where L_c is the sea surface correlation length, θ_x , and θ_y are respectively the full along-track, and across-track width of the beam at the half power point. To finish, $T_k(y_p)$ can be expressed as,

$$T_k(y_p) = \begin{cases} \left(1 + \frac{\alpha_\sigma}{\alpha_y}\right) - \frac{y_p}{L_y \sqrt{k}} \tanh(2\alpha_y y_p L_y \sqrt{k}), & k > 0 \\ \left(1 + \frac{\alpha_\sigma}{\alpha_y}\right) - 2\alpha_y y_p^2, & k \leq 0 \end{cases} \quad \text{Eq. 5.2-34}$$

Omitting the slope dependence, g_l can be simplified to,

$$g_l = \sqrt{\frac{2\alpha_g}{1 + 4\left(\frac{L_x}{L_y}\right)^2 l^2 + 2\alpha_g \left(\frac{\sigma_z}{L_z}\right)}} \quad \text{Eq. 5.2-35}$$

Neglecting the mean sea surface height ($\langle z_o \rangle$), and the electromagnetic bias (z_{EM}) $P_{k,l}$ becomes

$$P_{k,l} = P_u \sqrt{g_l} \Gamma_{k,l} \left\{ f_o(g_l k) + \frac{\sigma_z}{L_\Gamma} T_k(y_p) g_l \sigma_s f_1(g_l k) \right\} \quad \text{Eq. 5.2-36}$$

Omitting the first order term function f_1 Eq.5.2-36 can be simplified to,

$$P_{k,l} = P_u \sqrt{g_l} \Gamma_{k,l} f_o(g_l k) \quad \text{Eq. 5.2-37}$$

Expressing $f_o(g_l k)$ as a combination of Bessel functions (Gommenginger et al., 2012 , and Ray et al., 2012),

$$f_o(\xi) = \int_0^{+\infty} e^{-\frac{1}{2}(\xi - v^2)^2} dv = \frac{\pi}{2\sqrt{2}} \left(\frac{1}{4}\xi^2\right)^{1/4} \left[I_{-\frac{1}{4}}^{sc}\left(\frac{1}{4}\xi^2\right) + \text{sign}(\xi) I_{\frac{1}{4}}^{sc}\left(\frac{1}{4}\xi^2\right) \right] \quad \text{Eq. 5.2-38}$$

being I_v^{sc} the Scaled Spherical Modified Bessel function, defined as,

$$I_v^{sc}(z) = e^{-|z|} I_v(z) \quad \text{Eq. 5.2-39}$$

Considering this, Eq.5.2-37, becomes,

$$P_{k,l} = P_u \sqrt{g_l} \Gamma_{k,l} e^{-\frac{1}{4}(g_l k)^2} \begin{cases} (-g_l k)^{\frac{1}{2}} K_{\frac{1}{4}}\left(\frac{1}{4}(g_l k)^2\right), & g_l k > 0 \\ \frac{\pi}{\sqrt{2}} (g_l k)^{\frac{1}{2}} \left(I_{-\frac{1}{4}}\left(\frac{1}{4}(g_l k)^2\right) + I_{\frac{1}{4}}\left(\frac{1}{4}(g_l k)^2\right) \right), & g_l k \leq 0 \end{cases} \quad \text{Eq. 5.2-40}$$

where g_l , and $\Gamma_{k,l}$ have been introduced previously. Additionally is important to consider that for large values of $g_l k$ the Bessel functions shall be approximated by,

$$I_{-p}(k) = I_p(k) \quad \text{Eq. 5.2-41}$$

$$I_p(k) = \frac{\exp(k)}{\sqrt{2\pi k}} \quad \text{Eq. 5.2-42}$$

5.3 Development choices and trade offs

The analytical model to compute the SAR altimeter waveform, will be initially based on the truncated version of the SAR waveform model implemented in SAMOSA-3, including the main improvements and updates done during the framework of CP40, it includes,

- Appropriated handing of the energy distribution over the different echoes of the delay-Doppler stack.
- Constant values of the PTR Gaussian approximations width, based on the S3 IPF. Those constant values are,
 - Azimuth PTR Gaussian approximation coefficient = 0.3831
 - Range PTR Gaussian approximation coefficient = 0.513
- Complete implementation of the SAMOSA-2 model.
- Appropriate estimation of the thermal noise.

On the other side, the default configuration for the production of the Level-2 data, will be,

- Reference Time for the International Atomic Time (TAI) Datation is 01/01/2000 00:00:00.
- Reference Ellipsoid is the Topex/Poseidon Ellipsoid.
- DDM SAR Power Model masked according to Range-Cell Migrated range bins.
- Levenberg-Marquardt Least Mean Squares Minimization Algorithm (LEVMar-LSE).
- No static bias applied to the range, wave height, and σ_o measurements.
- Doppler Shift Correction applied to the range measurements.
- Internal path delay not applied to the range measurements.

5.4 Data flow

Figure 5.4-1 represents the data flow proposed for the Sentinel-3 re-tracker.

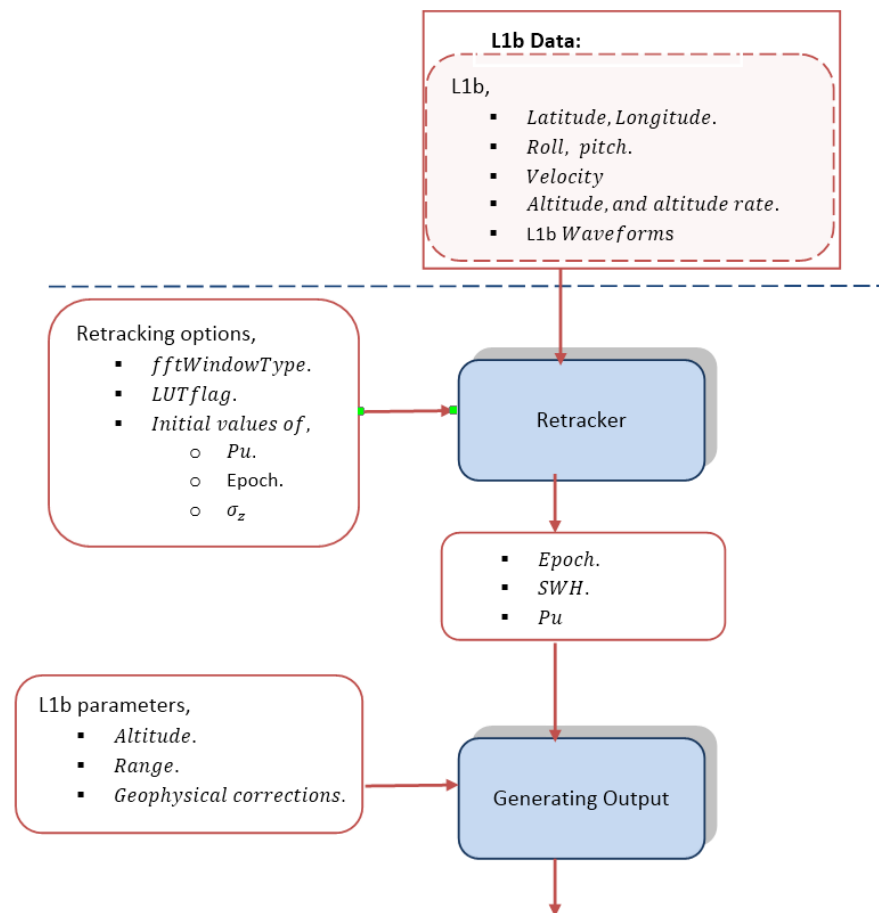


Figure 5.4-1 Block diagram of the data flow for the Sentinel-3 re-tracker.

5.4.1 Input data

From Figure 5.4-1 it can be noted that the re-tracker uses as inputs a configuration file and the L1B data.

5.4.1.1 Configuration file

The configuration file allows the user to select the different configuration parameters. The main configuration parameters are:

- L1B general Info: i.e., version of the L1B data.
- Geodetic parameters:
 - Semi-major axis of earth ($a = 6378137\text{m}$).
 - Semi-minor axis of earth ($b = 6356752.3142\text{m}$).
- Sentinel-3 parameters:
 - Central frequency (f_c).
 - Pulse Repetition Frequency (PRF).
 - Burst Repetition Interval (BRI).
 - Bandwidth (BW).
 - Pulse length (τ_p).

- Useful Pulse length (τ_u).
- Number of lags.
- Number of beams.
- Number of pulses.
- Number of Looks.
- Pitch bias (θ_{pitch}).
- Roll bias (θ_{roll}).
- Full along-track width of the half power (θ_x).
- Across-track width of the half power (θ_y).
- Re-tracking options:
 - Starting Waveform position for the re-tracking.
 - Waveforms Steps for the re-tracking.
 - A Flag indicating where to put the centre of the Doppler range.
 - 0 → centre is at the antenna centre.
 - 1 → centre is at the Doppler zero.
 - The window type used in the waveform model.
 - 0 → hamming.
 - 1 → boxcar.
 - LUT flag*:
 - 0 → don't use LUTs (i.e. SAMOSA-2).
 - 1 → use LUTs (i.e. SAMOSA-2).
 - 2 → don't use LUTs and don't use f1 (i.e. SAMOSA-3).
 - 3 → use LUTs and don't use f1 (i.e. SAMOSA-3).
 - 5 → use LUTs provided by ESA, generated from a linear combination of Bessel functions (i.e. SAMOSA-3).
 - Surface coherence length (only used for the sea slope PDF).
 - Surface slope flag:

*In the SAMOSA retracker, the waveforms are written as a function of basis functions, where f0 and f1 relates to the zero and first order function terms. Depending on the LUT flag, their computation varies.

When the LUT-flag is set up to 0, LUTs are not used. It means that the basis functions are computed according to Ray et al 2012, and defined as,

$$f_n(\xi) = \int_0^\infty e^{-\frac{1}{2}(\xi-u^2)^2} (\xi - u^2)^n du, \quad \text{Eq. 5.4-1}$$

If the argument $\xi \gg 1$ the integral in Eq.5.4-1 can be evaluated approximately. Letting $x = \xi - u^2$, and $du = -\frac{dx}{2\sqrt{\xi-x}}$, and assuming that the integral is only significant for values of x near zero, the limits of the integral can be extended to $+\infty$ without altering the integral significantly. Then keeping the lowest order nonzero term, the basis functions can be expressed as,

$$f_0(\xi) = \sqrt{\frac{\pi}{2\xi}}, \quad \text{Eq. 5.4-2}$$

$$f_1(\xi) = \sqrt{\frac{\pi}{2\xi}} \frac{1}{2\xi}, \quad \text{Eq. 5.4-3}$$

$$f_2(\xi) = \sqrt{\frac{\pi}{2\xi}}, \quad \text{Eq. 5.4-4}$$

$$f_3(\xi) = \sqrt{\frac{\pi}{2\xi}} \frac{3}{2\xi}, \quad \text{Eq. 5.4-5}$$

$$f_4(\xi) = \sqrt{\frac{\pi}{2\xi}} 3, \quad \text{Eq. 5.4-6}$$

In order to speed up the process, the computation of the f_n can be done by means of Lookup tables (LUTs).

Therefore, if LUT-flag is set-up to 1, f0 and f1 using Ray et al 2012 approach. Accounting that the functions $f_n(\xi)$ are not dependent on any parameter of the system, it is possible the use of LUTs to speed the process. Being ξ_b , ξ_a the range of values in which it is needed to know the functions, the first step is compute the functions using an accurate method at a sequence of N equally spaced ξ values,

$$\xi_i = \xi_a + \frac{\xi_b - \xi_a}{(N-1)} i, \quad \text{Eq. 5.4-7}$$

The values are computed as

$$T_{n,i} = f_n(\xi_i), \quad \text{Eq. 5.4-8}$$

and then stored in memory in a lookup table. Then f0 and f1 are computed using the lookup table as follows. Firstly, is computed the index as,

$$i = \text{floor} \left[\frac{\xi - \xi_a}{\xi_b - \xi_a} (N - 1) \right], \quad \text{Eq. 5.4-9}$$

where ξ_b , ξ_a are the range of values in which is needed to know the functions, and N is a sequence of values equally spaced. Thus, f_n is computed as,

$$f_n(\xi) \approx \xi_i G_{n,i} + H_{n,i} \quad \text{Eq. 5.4-10}$$

where $G_{n,i}$ and $H_{n,i}$, are computing using as,

$$G_{n,i} \approx \frac{T_{n,i+1} - T_{n,i}}{\xi_{i+1} - \xi_i} \quad \text{Eq. 5.4-11}$$

and,

$$H_{n,i} \approx T_{n,i} - \xi_i G_{n,i} \quad \text{Eq. 5.4-12}$$

where $T_{n,i}$ is the look-up table stored (Eqn. 5.4-8)

When LUT-flag is set up to 2, LUTs are not used and only f0 is computed based on the integral definition (Eqn. 5.4-1 and 5.4-2).

When LUT-flag is set up to 3, only f0 is computed based using LUTs as it has described previously (Eqn. 5.4-8 – Eqn. 5.4-12).

Finally, when LUT-flag is set up to 5, f0 is computed as,

$$f(\xi) \approx (\xi_i - LUT_FO_{0,j}) * \frac{LUT_FO_{0,j+1} - LUT_FO_{0,j}}{LUT_FO_{1,i+1} - LUT_FO_{0,i}} + LUT_FO_{1,j} \quad \text{Eq. 5.4-13}$$

Where LUT_F0 is taken from an ESA LUT (see Gommenginger et al 2013).

The waveform in the SAMOSA retracker is computed as,

$$W = \text{amp}(t_0 + t_1), \quad \text{Eq. 5.4-14}$$

Where amp is computed as a function of the scaling parameter (g), and the antenna gain (Go), whereas the computation of the t_0 and t_1 depends on if the skewness is accounted for, and on the LUT_flag (see section 5.4.2.4.2 of this ATBD document).

5.4.1.2 L1b data

L1b Data Products generated by isardSAT from CryoSat-2 SAR FBR (Full Bit Rate) Products after the processing of the Delay-Doppler Data will be used. The main parameters added on each iteration of the re-tracker are:

- Time info.
 - Time (i.e. time at surface of the SAR measurement).
 - Day (i.e. day elapsed since 01/01/2000 00:00:00).
 - Seconds (i.e. seconds in the day UTC).
- Orbital and attitude info.
 - Latitude.
 - Longitude.
 - Altitude.
 - Altitude rate.
 - Roll.
 - Pitch.
- Velocity (x, y, and z components).
- Look angle start and stop.
- Doppler angle start and stop

Altitude command COR2, and AGC code for Ku Band.

- Surface type.
- Altimeter Range.
 - Range.
 - USO frequency drift correction.
 - Internal path correction.
- Sigma0 scaling factor.
- Geophysical corrections.
 - Dry Tropospheric.
 - Wet Tropospheric.
 - Inverse Barometric.
 - GIM Ionospheric.
 - Model Ionospheric.
 - Ocean Equilibrium Tide.
 - Long Period Ocean Tide.
 - Ocean Load Tide.
 - Solid Earth Tide.
 - Geocentric Polar Tide.

5.4.2 Ancillary information

Figure 5.4-2 shows a more detailed block diagram for the retracker. In the initial steps, the configuration parameters are set up according to the configuration file (see previous section), the main constants and the starting values for the retracker are defined, and data from the L1b file is read (see previous section). Additionally, the main constants that will be used during the computation of the Waveform are defined. After that the Doppler Beams are computed, the SAR Waveform is normalized, and the noise is estimated.

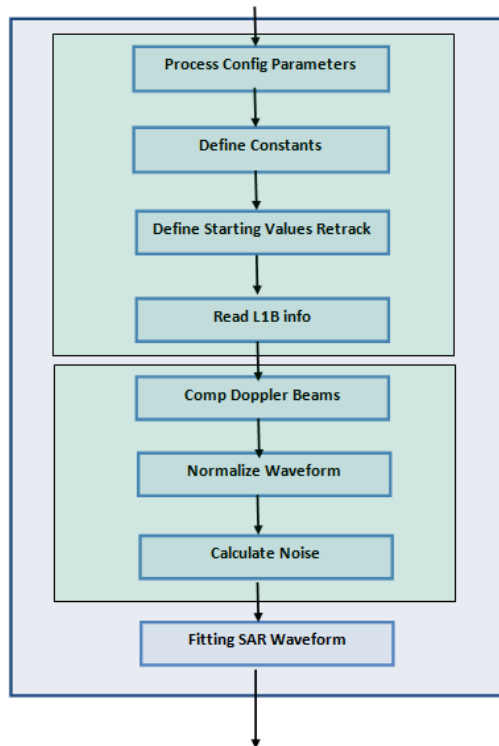


Figure 5.4-2 Block diagram for the Sentinel-3 retracker based on SAMOSA-3.

5.4.2.1 Calculation of Doppler Beams

In this step the Doppler beams of each burst are calculated. Hence, for each angle in the beam stack, the corresponding Doppler frequency is computed as (Gommenginger et al., 2013-2015),

$$DopplerFreqStack = \frac{2v_s}{\lambda} \cos(BeamAngleStack) \quad \text{Eq. 5.4-15}$$

where v_s is the satellite velocity (obtained in the previous step from the L1b file) and λ is the wavelength (defined during the retracking configuration). On the other side, the *BeamAngleStack* is the array of angles of the Doppler beams used for the multilooking, given by,

$$BeamAngleStack = \frac{\pi}{2} + d\theta((N_{looks} + 1) - \frac{N_{looks}}{2}) \quad \text{Eq. 5.4-16}$$

where

$$d\theta = \frac{vs * BRI}{h * \alpha} \quad \text{Eq. 5.4-17}$$

with vs being the satellite velocity, BRI the Burst Repetition Interval, h the satellite altitude, and α the Earth Curvature expressed as,

$$\alpha = 1 + \frac{h}{R_e} \quad \text{Eq. 5.4-18}$$

where R_e is the earth radius, given by,

$$R_e = \sqrt{a^2 \cos^2 \theta_{plat} + b^2 \sin^2 \theta_{plat}} \quad \text{Eq. 5.4-19}$$

where a is the semi-major axis of earth, b is the semi-minor axis of earth, and θ_{plat} is the ground cell latitude.

Once the Doppler beams of each burst has been computed, the Doppler frequency can be expressed as,

$$dopplers = \frac{DopplerFreqStack}{dfa} \quad \text{Eq. 5.4-20}$$

where dfa is a scale factor that is applied to relate the Doppler frequency to the index l , defined by,

$$dfa = \frac{PRF}{N_{beams}} \quad \text{Eq. 5.4-21}$$

PRF denotes the Pulse Repetition Frequency, and N_{beams} the number of beams.

From Eq. 5.4-15 the first and last Doppler beam can be computed as,

$$Doppler_{start} = (2 * vs / \lambda) * \cos(\pi/2 - \text{ang_start} + \text{dop_start}) \quad \text{Eq. 5.4-22}$$

$$Doppler_{end} = (2 * vs / \lambda) * \cos(\pi/2 - \text{ang_stop} + \text{dop_stop}) \quad \text{Eq. 5.4-23}$$

where angle_start/stop (are the Look angle of the first and last contributing look (non-0 weight) to the L1B waveform), and dop_start/stop (the Doppler angle of the first and last contributing look (non-0 weight) to the L1B waveform), obtained from the L1b files.

*Note that a zero-mask is applied to the stack before multilooking. It includes the geometry corrections mask to avoid wrapping effects. Each element of the mask refers to a look in the stack and indicates the index of the first sample set to zero. When a specific look or beam shall not be considered at all in the multilooking the value is set to -1 (i.e. $\text{dopplers} = \text{dopplers}[\text{stack_mask} > -1]$).

5.4.2.2 Normalize Waveform

In this step the 20Hz L1B SAR Waveform is normalized by the maximum Waveform amplitude as,

$$\text{Waveform_Norm} = \frac{\text{Waveform}}{(\text{Waveform_max})} \quad \text{Eq. 5.4-24}$$

where wavform_max is computed using a sliding window as,

$$\text{Waveform_max} = \max_j \left\{ \frac{\sum_i \text{Waveform}(i)}{\sum_i 1} \right\} \quad \text{Eq. 5.4-25}$$

with

$$\begin{aligned} j &\in [Wf_Norm_first, Wf_Norm_Last - Wf_Norm_Av] \\ i &\in [j, j + Wf_Norm_Av] \end{aligned} \quad \text{Eq. 5.4-26}$$

where Wf_Norm_first is the index of the first sample in the measured waveform to search the maximum amplitude, Wf_Norm_last is the index of the last sample in the measured waveform to search the maximum amplitude, and Wf_Norm_av is the width of the sliding window.

5.4.2.3 Calculate Noise level

Estimation of the thermal noise is a key parameter in the retracking of the SAR waveforms, since it affects directly the estimation of the SWH. The noise level was obtained as the average value of the first SAR waveforms lags, typically lags from 11 to 21. However, this approach does not consider the impact that the SWH can have on the leading edge and on the amplitude of the averaged SAR waveform.

Within the framework of the original CP40 contract, an initial estimation and introduction of the thermal noise in SAMOSA was conducted (Egido, 2014). In this work an empirical method was proposed, measuring the noise level directly in the SAR-Waveform considering the range gates located before the leading edge, and the variability in its position. The initial approach has been optimised during the CP40 project (Martin and Repucci, 2015).

Thus, the current approach implemented in the retracker, proposes to estimate the beginning of the leading edge, subtracting two times the lag distance ($d1$) between the peak of the waveform and the half-peak point of the waveform. After that an extra margin of 16 lags is added, in order to ensure that the leading edge will not be considered as a noise. Figure 5.4-3 represents how the noise floor is estimated.

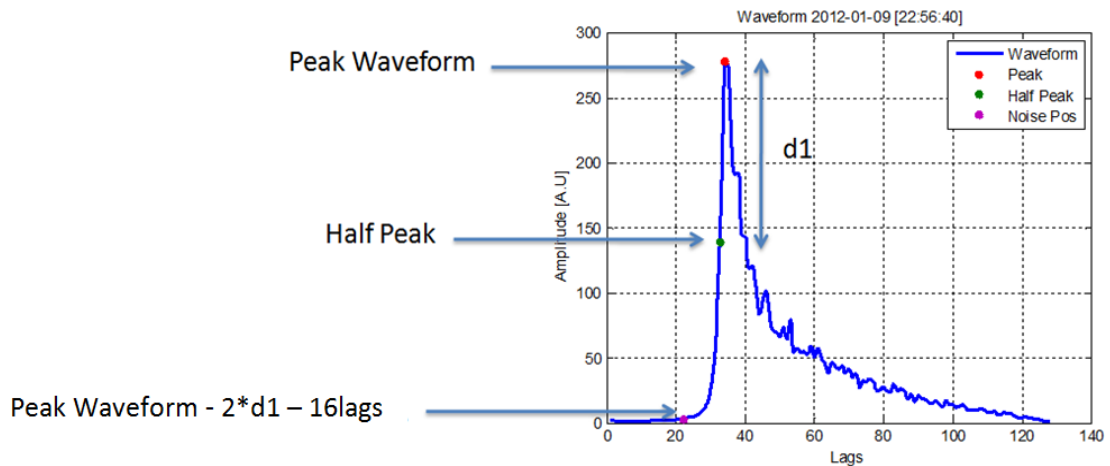


Figure 5.4-3 Empirical approach for estimate the Waveform noise floor.

The main equations to compute the thermal noise are

$$leadingEdgeSpan = 2 * (WaveformPeakPos - HalfPowePos) \quad \text{Eq. 5.4-27}$$

$$leadingEdgeStartingPos = WaveformPeakPos - leadingEdgeSpan \quad \text{Eq. 5.4-28}$$

$$NoisePos = leadingEdgeStartingPos - (16) \quad \text{Eq. 5.4-29}$$

$$Noise_Floor = \begin{cases} \text{mean}(\text{Waveform}[NoisePos - 1:NoisePos + 1]), & NoisePos > 1 \\ \text{mean}(\text{Waveform}[1:2]), & NoisePos \leq 1 \end{cases} \quad \text{Eq. 5.4-30}$$

5.4.2.4 Fitting the SAR Waveform

In order to retrieve the geophysical parameters of interest (i.e. Sea Surface Height (SSH), Significant Wave Height (SWH), and σ_o), the 20Hz L1B SAR waveform is fitted with the theoretical multi-look waveform generated by the model developed within SAMOSA. The retracker is based on a non-linear least square algorithm that relies on a Levenberg-Marquardt minimization method.

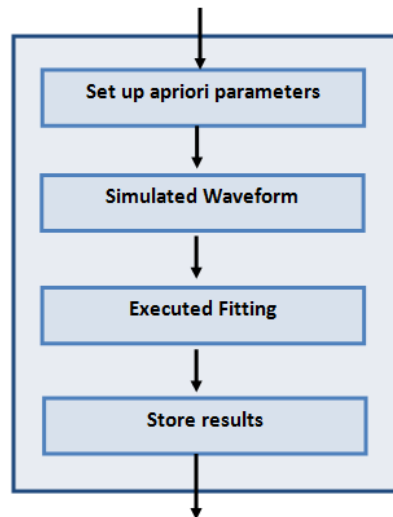


Figure 5.4-4 Block diagram of the retracker module.

5.4.2.4.1 Set up a priori parameters

From Figure 5.4-4 the first step followed during the SAR Waveform fitting is the set-up of the a priori parameters. These parameters are,

- Doppler step.
- Latitude.
- SWH.
- Lag.
- Doppler Start.
- Doppler End.
- Fft Window type.
- Doppler Centre.
- LUT Flag.
- Altitude.
- Satellite velocity.
- Roll.
- Pitch.
- Noise Level.
- Pu.

5.4.2.4.2 Simulating the SAR Waveform

The second step accounts for the simulation of the SAR Waveform. Figure 5.4-5 summarizes the main steps involved in the Waveform computation. First of all, the main parameters that will be used in the computations are defined and added from the L1B file. Those parameters and constants are,

- Semi-major axis of earth ($a = 6378137\text{m}$).
- Semi-minor axis of earth ($b = 6356752.3142\text{m}$).
- Speed of light ($c = 299792458\text{ m/s}$).
- Central frequency of chirp (f_c).
- Number of pulses per burst (N_b).
- Bandwidth (BW).
- Transmitted pulse length (τ_p).
- Useful pulse length (τ_u).
- PRF.
- Pitch bias (θ_{pitch}).
- Roll bias (θ_{roll}).
- Along-track 3 dB Beamwidth (θ_x).
- Across-track 3 dB Beamwidth (θ_y).

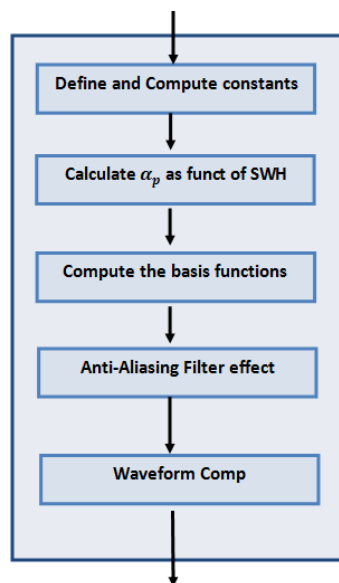


Figure 5.4-5 Block diagram of Waveform computation.

Once the main constants and parameters have been defined and obtained from the L1B file, the following constants are computed for further processing,

The Earth radius (R_e), defined as a function of the geodetic parameters a and b (Gommenginger, et al., 2013-15),

$$R_e = \sqrt{a^2 \cos^2 \theta_{plat} + b^2 \sin^2 \theta_{plot}}, \quad \text{Eq. 5.4-31}$$

The surface slope of the sea surface due to elliptical earth (s) (Gommenginger, et al., 2013-15),

$$s = \left(-\left(\frac{a^2 - b^2}{2R_e^2} \right) \sin(2lat) - \left(\frac{-h_{rate}}{v_s} \right) \right) \quad \text{Eq. 5.4-32}$$

The Earth curvature effect (α),

$$\alpha = 1 + \frac{h}{R_e} \quad \text{Eq. 5.4-33}$$

The frequency sweep rate,

$$beta = \frac{BW}{\tau_p} \quad \text{Eq. 5.4-34}$$

The burst period,

$$T_b = \frac{N_b}{PRF} \quad \text{Eq. 5.4-35}$$

The along-track length scale (L_x), across-track length scale (L_y), and height length scale (L_z),

$$L_x = \frac{ch}{2v_s f_c T_b} \quad \text{Eq. 5.4-36}$$

$$L_y = \sqrt{\frac{ch}{\alpha \cdot beta \cdot \tau_u}} \quad \text{Eq. 5.4-37}$$

$$L_z = \frac{c}{2 \cdot beta \cdot \tau_u} \quad \text{Eq. 5.4-38}$$

The Doppler bin number (l_s)

$$l_s = \frac{sh}{\alpha L_x} \quad \text{Eq. 5.4-39}$$

The beam mis-pointing (x_p and y_p)

$$\begin{aligned} x_p &= h\theta_{pitch} \\ y_p &= -h\theta_{roll} \end{aligned} \quad \text{Eq. 5.4-40}$$

The height variation length scale (L_g)

$$L_g = \frac{\alpha h \theta_y^2}{16 \ln 2} \quad \text{Eq. 5.4-41}$$

Finally α_x , α_y , and α_σ are defined as, (Ray et al., 2012, and Gommenginger et al., 2012),

$$\alpha_x = \frac{8 \ln(2)}{h^2 \theta_x^2} \quad \text{Eq. 5.4-42}$$

$$\alpha_y = \frac{8 \ln(2)}{h^2 \theta_y^2} \quad \text{Eq. 5.4-43}$$

$$\alpha_\sigma = \left(\frac{L_c}{2\sigma_z h} \right)^2 \quad \text{Eq. 5.4-44}$$

Once the main constants have been defined the variable Point Target Response (PTR) width (α_p) is defined as a function of the Significant Wave Height (SWH) based on the method proposed by Dinardo, such that α_p can be analytically defined as,

$$\alpha_{p_{az}} = 0.3831, \quad \alpha_{p_r} = 0.513 \quad \text{Eq. 5.4-45}$$

After that, a scaling parameter g is computed as,

$$g = \frac{1}{\sqrt{\alpha_p^2 + \alpha_p^2 2G^2 + \sigma^2}} \quad \text{Eq. 5.4-46}$$

where α_p has been defined previously, and G and σ are given by,

$$G = 2 \left(\frac{L_x}{L_y} \right)^2 (1 - l_s) \quad \text{Eq. 5.4-47}$$

$$\sigma = \frac{\sigma_z}{L_z} \quad \text{Eq. 5.4-48}$$

where l is a scalar integer giving the delay bin value. On the other side, l_s is given by,

$$l_s = \frac{x_s}{L_x} \quad \text{Eq. 5.4-49}$$

with x_s equal to,

$$x_s = \frac{sh}{L_x \alpha} \quad \text{Eq. 5.4-50}$$

Now the scaled distance is expressed as,

$$g_x = g * x_{\text{corrected}} \quad \text{Eq. 5.4-51}$$

where $x_{\text{corrected}}$ is,

$$x_{\text{corrected}} = x - d\tau \quad \text{Eq. 5.4-52}$$

And x is a vector containing the delay bins values, being $d\tau$ an extra delay.

Now the basis functions are computed. Firstly, the antenna gain slope (T_{ky}), which is given by (Ray et al., 2012, and Gommenginger et al., 2013-15),

$$T_{ky} = \begin{cases} \left(1 + \frac{\alpha_\sigma}{\alpha_y}\right) - \frac{y_p}{y_k} \tanh(2\alpha_y y_p y_k), & x_{\text{corrected}} > 0 \\ \left(1 + \frac{\alpha_\sigma}{\alpha_y}\right) - 2\alpha_y y_p^2, & x_{\text{corrected}} \leq 0 \end{cases} \quad \text{Eq. 5.4-53}$$

where y_k is the across-track position from the delay gate,

$$y_k = L_y \sqrt{x_{\text{corrected}}} \quad \text{Eq. 5.4-54}$$

In a similar way, the along-track position from the Doppler bin number can be written as,

$$x_l = L_x e_l \quad \text{Eq. 5.4-55}$$

Then the antenna Gain is computed as (Gommenginger et al., 2013-15),

$$G_o = \exp\left(-\alpha_x(x_l - x_p)^2 - \alpha_y y_p^2 - \alpha_\sigma x_l^2 - (\alpha_y + \alpha_\sigma) y_k^2\right) \cosh(2\alpha_y y_p y_k) \quad \text{Eq. 5.4-56}$$

From the scaling parameter (g), and the antenna Gain (G_o), the overall waveform amplitude is computed as,

$$\text{amp} = \sqrt{g} G_o \quad \text{Eq. 5.4-57}$$

and then the waveform as,

$$W = \text{amp}(t_o + t_1) \quad \text{Eq. 5.4-58}$$

where,

$$t_o = \begin{cases} f_o, & \lambda_s = 0 \\ f_o + \left(\frac{\lambda_s}{2}\right) g_s^3 f_1 - \left(f_1 - \left(\frac{\lambda_s}{6}\right) g_s^3 f_3\right), & \lambda_s \neq 0 \end{cases} \quad \text{Eq. 5.4-59}$$

with

$$g_s = g\sigma \quad \text{Eq. 5.4-60}$$

and

$$t_1 = \begin{cases} \frac{\sigma_z}{L_g} T_{ky} g_s f_1, & \text{LUT flag} > 2 \\ 0, & \text{LUT flag} \leq 2 \\ -\frac{\sigma_z}{L_g} T_{ky} \left(\left(\frac{\lambda_s}{2}\right) (1 - g_s^2) g_s^2 f_o - g_s f_1 + \left(\frac{\lambda_s}{2}\right) (1 - 2g_s^2) g_s^2 f_2 + \left(\frac{\lambda_s}{6}\right) g_s^4 f_4 \right), & \lambda_s \neq 0 \end{cases} \quad \text{Eq. 5.4-61}$$

5.4.3 Output

An L2 data product output will be generated for each L1b file. The file name will be [INPUT_FILENAME].RES.dat_stl.nc.

The L2 data product will provide,

- Time info.
 - Time (i.e. time at surface of the SAR measurement).
 - Day (i.e. day elapsed since 01/01/2000 00:00:00).
 - Seconds (i.e. seconds in the day UTC).
- Orbital and attitude info.
 - Latitude.
 - Longitude.
 - Altitude.
 - Altitude rate.
 - Roll.
 - Pitch.
- Velocity (x, y, and z components).
- Altitude command COR2, and AGC code for Ku Band.
- Surface type.
- Altimeter Range.
 - Range.
 - USO frequency drift correction.
 - Internal path correction.
- Sigma0 scaling factor.
- Geophysical corrections.
 - Dry Tropospheric.
 - Wet Tropospheric.
 - Inverse Barometric.
 - GIM Ionospheric.
 - Model Ionospheric.
 - Ocean Equilibrium Tide.
 - Long Period Ocean Tide.
 - Ocean Load Tide.
 - Solid Earth Tide.
 - Geocentric Polar Tide.
- Retracker Outputs.
 - SSH non corrected.
 - SSH corrected.
 - SWH.
 - Pu.
- Misfit, which is calculated as the root mean square of the sum of the squared residuals scaled by the number of bins in the waveform (Cotton and Passaro, 2016).

$$misfit = 100 * \sqrt{\frac{1}{104} \sum (residual^2)} \quad \text{Eq. 5.4-62}$$

where the residual is the difference between the fitting curve and the real waveform at each bin scaled by the maximum of the waveform values.

6 References

Amarouche, L., P. Thibaut, O.-Z. Zanifé, J.-P. Dumont, P. Vincent, and N. Steunou, Improving the Jason-1 ground retracking to better account for attitude effects, *Mar. Geod.*, 27, 171–197, doi: 10.1080/01490410490465210, 2004.

Boy, F., J.-D. Desjonquieres, N. Picot, T. Moreau, S. Labroue, J.-C. Poisson, & P. Thibaut, (2012): Cryosat Processing Prototype: LRM and SAR processing on CNES side. Ocean Surface Topography Science Team 2012, Venice, 27-28 Sept 2012, Available from: <http://www.aviso.oceanobs.com/en/courses/sciteams/ostst-2012.html>.

Cipollini, P., (2016a), SAR Altimetry Scientific Review, SCOOP Project Document SCOOP-TN-1, April 2016.

Cipollini, P., (2016b), SCOOP Requirements Baseline, SCOOP Project Document SCOOP-RB, April 2016

Cotton, P.D., (2015a), SCOOP Project Plan v1.0, SCOOP Project Document SCOOP-PMP-01, 10/11/15.

Cotton P. D., (2015b), SCOOP Kick Off Meeting Minutes. Cotton, P.D., SCOOP Project Document SCOOP-MOM_001,09/1015

Cotton. D. and M. Passaro, (2016), CP40 Cryosat Plus for Oceans (CCN1) – WP3000 – SAMOSA SAR Retracker improvements Assessment of Evaluation Data Set.

Cotton P. D. et al., (2015), SCOOP Proposal: SAR Altimetry Coastal and Open Ocean Performance Exploitation and Roadmap Study, Proposal in Response to ESA ITT AO/1-8080/14/I-BG, in 5 parts, January 2015

Cumming, I.G.; Wong, F.H., (2005) *Digital Processing of Synthetic Aperture Radar Data. Algorithms and Implementation*. Boston, MA: Artech House.

Curlander, John C., and Robert N. McDonough. (1991) *Synthetic aperture radar*. New York, NY, USA: John Wiley & Sons, 1991.

Dinardo, S., 2013, Technical Note to the SAMOSA Team for CP40 Round Robin Exercise, CP40 Internal Project Document

Fenoglio-Marc, L., S. Dinardo, R. Scharroo, A. Roland, M. Dutour Sikiric, B. Lucas, M. Becker, J. Benveniste, R. Weiss, 2015, The German Bight: a validation of CryoSat-2 altimeter data in SAR mode, *Advances in Space Research* 55(11), May 2015, DOI: 10.1016/j.asr.2015.02.014

Garcia. E.S., Sandwell, D. T., and Smith, H.F. (2014), Retracking CryoSat-2, Envisat and Jason-1 radar altimetry waveforms for improved gravity field recovery, *Geophysical Journal International* Advance Access, doi: 10.1093/gji/ggt469.

Garcia, P., 2018, “WP4000: Coastal Processing Phase 2” Presentation to SCOOP Acceptance Review, Toulouse, 3rd December 2018.

Gommenginger, C., C Martin-Puig, I Amarouche and R.K. Raney, (2013), Review of State of Knowledge for SAR altimetry over ocean, EUMETSAT Study Report EUM/RSP/REP/14/749304, V. 2.2, 21 Nov 2013, 57 pp

Gommenginger, C., Martin-Puig. C., Srokosz. M., Caparrini. M, Dinardo. S., and Lucas. B., (2013), SAMOSA3 WP2300: Detailed Processing Model of the Sentinel-3 SRAL SAR altimeter ocean waveform retracker. Version 2.3.0.

Gommenginger, C., Martin-Puig. C., Srokosz. M., Caparrini. M, Dinardo. S., and Lucas. B., (2015), SAMOSA3 WP2300: Detailed Processing Model of the Sentinel-3 SRAL SAR altimeter ocean waveform retracker. Version 2.5.0.

Egido. A., (2012), CP40 Cryosat Plus for Oceans: D4.1 Algorithm Theoretical and Validation Document Ray. C, Martín-Puig, C., 2012, SAMOSA (CCN2) – SAMOSA models trade-off technical note.

Jensen, J. R. (1999), Radar altimeter gate tracking: Theory and extension, *IEEE Trans. Geosci. Rem. Sens.*, 37(2), 651–658.

Lambers, J, (2011-12) "The Method of Steepest Descent", Summer Session, Lecture 10 Notes.

MacArthur, J. L. "Seasat-A radar altimeter design description," Rep. SDO-5232. *Appl. Phys. Lab.*: Johns Hopkins Univ., Baltimore, Md., 1978.

Makhoul, E. (2019), SAR Level-2 Algorithms Technical Baseline Document (ATBD), SCOOP Project Technical Note, 4 February 2019.

Marquardt, D. (1963). "An Algorithm for Least-Squares Estimation of Nonlinear Parameters". *SIAM Journal on Applied Mathematics* 11 (2): 431–441. doi:10.1137/0111030.

Martin, F., Repucci, A., (2015), CP40 Cryosat Plus for Oceans: WP3000-Improved Estimation of the Thermal Noise in the SAMOSA retracker.

Martin-Puig, C., J. Marquez, G. Ruffini, R. K. Raney, & J. Benveniste 2008: SAR Altimetry applications over water. Proceedings of the ESA SeaSAR workshop, Frascati, Italy, January 2008.

Ortega, J.M, and Rheinboldt, W.C, Iterative Solution of Nonlinear Equations in Several Variables, Academic Press, New York, 1970.

Phalippou, L.V. Enjolras, (2007): "Retracking of SAR altimeter ocean power waveforms and related accuracies of the retrieved sea surface height, significant wave height and wind speed." Igarss: 2007 IEEE International Geoscience and Remote Sensing Symposium, Vols 1-12, 3533-3536.

Prats-Iraola, P.; Scheiber, R.; Rodriguez-Cassola, M.; Mittermayer, J.; Wollstadt, S.; De Zan, F.; Brautigam, B.; Schwerdt, M.; Reigber, A.; Moreira, A., (2014) "On the Processing of Very High Resolution Spaceborne SAR Data," in *IEEE Transactions on Geoscience and Remote Sensing*, vol.52, no.10, pp.6003-6016, Oct. 2014

Raney, R. K. (1998) "The delay/Doppler radar altimeter," in *IEEE Transactions on Geoscience and Remote Sensing*, vol.36, no.5, pp.1578-1588, Sep 1998

Ray, C., (2012) SAMOSA models trade-off technical note, SAMOSA3 CCN2 WP2100.

Ray, C., C. Martin-Puig, M.-P. Clarizia, G. Ruffini, S. Dinardo, C. Gommenginger, & J. Benveniste 2013: SAR Altimeter Backscattered Waveform Model. *IEEE Transactions on Geoscience and Remote Sensing*.

Rodriguez, E., (1988), "Altimetry for Non-Gaussian Oceans. Height Biases and Estimation of Parameters," *Journal of Geophysical Research*, vol. 93. No. 11, pp. 14,107-14,120, 1988.

Sandwell, D. T., E. Garcia, & W. H. F. Smith, 2011: Improved Marine Gravity from Cryosat and Jason-1. Ocean Surface Topography Science Team 2011, San Diego, 19-21 Oct 2011,

<http://www.aviso.oceanobs.com/en/courses/sci-teams/ostst-2011.html>.

Scharroo, R., (2014), "RADS RDSAR Algorithm Theoretical Basis Document", v 0.3, Technical Note for ESA CP4O project, available at:

http://www.satoc.eu/projects/CP4O/docs/tud_rdsar_atbd.pdf

Scharroo, R., W. H. F. Smith, and M. C. Naeije (2012a), Validation of CryoSat test data set over open oceans (LRM and FDM, Level 1 and 2), Tech. rep., Altimetrics LLC.

Scharroo, R., W. H. F. Smith, and M. C. Naeije (2012b), Updated validation of CryoSat test data set over open oceans (LRM and FDM, Level 1 and 2), Tech. rep., Altimetrics LLC.

Scharroo, R., W. H. F. Smith, and M. C. Naeije (2012c), Re-updated validation of CryoSat test data set over open oceans (LRM and FDM, Level 1 and 2), Tech. rep., Altimetrics LLC.

Scharroo, R., W. H. F. Smith, J. L. Lillibridge, and E. W. Leuliette (2012d), Calibration and validation of combined conventional and reduced SAR mode data over oceans and in the coastal regime, presented at Sixth Coastal Altimetry Workshop, Riva del Garda, Italy, 20-21 September 2012.

Scharroo, R., W. H. F. Smith, J. L. Lillibridge, and E. W. Leuliette (2012e), Global Cal/Val of CryoSat-2 LRM and SAR data over oceans, Ocean Science Topography Science Team Meeting, Venice, Italy, 27-29 September 2012.

Scharroo, R., W. H. F. Smith, E. W. Leuliette, and J. L. Lillibridge (2013a), The performance of CryoSat-2 as an ocean altimeter, in Proc. of the CryoSat-2 Third User Workshop, Dresden, 12-14 March 2013, Eur. Space Agency Spec. Publ., ESA SP-717, p. 5 pp.

Scharroo, R., W. H. F. Smith, E. W. Leuliette, and J. L. Lillibridge (2013b), CryoSat-2: The other ocean altimeter, ESA Living Planet Symposium, Edinburgh, Scotland, 9-13 September 2014.

Smith, W.H.F, and R. Scharroo (2011), Re-tracking range, SWH, sigma-naught, and attitude in CryoSat conventional ocean data, OST Science Team meeting, San Diego, 19 - 21 Oct 2011: http://www.aviso.oceanobs.com/fileadmin/documents/OSTST/2011/oral/01_Wednesday/Splinter%20IP/03%20Smith%20WHFSmith_IP_CS2_2.pdf

Smith, W. H. F., and R. Scharroo (2014), Waveform aliasing in satellite radar altimetry, IEEE Trans. Geosci. Rem. Sens., 53 (4), doi:10.1109/TGRS.2014.2331193.

Smith, W. H. F. and Scharroo, R., "Retracking range, SWH, sigma-naught, and attitude in CryoSat conventional ocean data", OSTST, San Diego, 19-21 October 2011.

Valenzuela. G. R. (1977), Theory for the interaction of electromagnetic and oceanic waves – a review.

Additional to these documents, the Sentinel-6 Algorithm Technical Baseline Description (ATBD) is a reference for all the methodologies applied in the L1B processing. Such document is still internal to the S6 project but will be ready before the conclusion of this project.

7 Symbols

Symbol	Definition
A	Amplitude (from altimeter waveform)
$A_{surf}(b')$	Area of the surface for the specific beam b' within stack
b	Surface dependent index or beam index within a burst
b'	Beam dependent index after stack masking
c	Speed of light.
f, f_d	Frequency, Doppler frequency
G	Waveform scale factor, or (with subscripts) its various components, e.g. gain, amplitude or attenuation corrections
G_{AGC}	AGC setting, properly corrected from integer values (dB)
G_{amp}	Amplitude determined by the re-tracker based on the waveforms normalised to have a peak value of 65535, converted to dB.
$G_\eta, G_h, G_\xi, G_{SWH}$	Attenuation corrections: for the flattening of the Earth, because of non-nominal altitude; because of off-nadir angle; because of SWH
G_N	Nominal attenuation at nominal altitude ($h_N=735$ km) and with zero off-nadir angle (dB)
G_0	Antenna gain at boresight
$G_{S,SAR}$	Processor gain in SAR mode (125.8 dB)
G_{TxRx}	Transmitter and receiver gain (dB)
G_{Tx}	Transmit power (dBW)
G_W	Waveform scale factor needed to normalise the PLRM waveforms (dB)
$ \vec{h}(l) $	Norm of the real height above the surface 'l'
h, \dot{h}	Orbital altitude, altitude rate
$H_{mask}(b', n')$	Mask at stack level
i	Index integer
$I_0(z)$	Bessel Function
$I(p,k), Q(p,k)$	Complex waveform components
k_{σ^0}	Sigma0 scaling factor average over the different beams
$k_\sigma(b')$	Sigma0 scaling factor per beam within the stack
$K(\xi^2)$	MIs-pointing (from altimeter waveform)
$[lon, lat, alt]$	Position in the geographical (geodetic) coordinates
L_c, L_x, L_y, L_z	Ocean correlation length, Length scale along track, across track and height length scale
n	Range-sample dependent index

N	Noise level (from altimeter waveform)
N_b	Number of beams per burst
N_{bs}	Number of beams pointing to a specific location
N_p	Number of pulses per burst
N_s	Number of samples in range
p	Pulse dependent index
P_{surf}	Surface impulse response
P_{TX}	Transmitted power
r	Range, range correction
$ \vec{r}(b') $	Norm of the range vector per Doppler beam pointing to a specific surface
R	mean radius of the Earth (6371 km)
R_e	Earth radius
s	Width (from altimeter waveform)
\vec{v}_s	Satellite's velocity vector
$W(k)$	Waveform power for sample k
$\vec{w}_{sat \rightarrow surf}$	Vector from the satellite position for a given burst to the specific surface location
$W(p)$	Azimuth dependent weighting or window
x_0	Epoch (from altimeter waveform)
$[x, y, z]$	Position in the Cartesian coordinates
z	height
z_o	Mean sea surface height
z_{EM}	Electro-magnetic bias
ZP	zero-padding or oversampling factor used in the range-compression via FFT
α	Earth curvature effect, angle of sight
α_p	Point Target Response width
β	Antenna beam width
γ	antenna aperture parameter
$\Delta r(b')$	Slant range variation per beam within the stack
$\Delta s_{wd}(b')$	Window delay misalignment correction (in samples)
η	Sea surface height relative to the mean
$\theta_{beam}(b, p)$	Beam angle (or phase) for beam index b and pulse index p
θ, θ_c	Angular azimuth beam resolution, beam angle
θ_x, θ_y	Along track and across track beam width
θ_{plat}	Planetographic latitude
λ	(carrier) wavelength

ξ	off-nadir angle
ρ	Subscript referring to echo or pulse number
$p(\eta)$	Probability density of the sea surface height
σ_0	Surface backscatter coefficient at normal incidence
σ_z	RMS of specular scattering points
σ_{slopes}^2	Variance of total sea surface slope
σ_z	Standard deviation of the sea surface height
τ, τ_B	Time delay, (burst) duration
τ_{wdref}	Reference window delay within the stack
$\tau_{wd}(b')$	Window delay associated with the b' beam and T_0 the clock period.
ϕ	Phase, or phase shift
$\psi_{gm_stack}(b', n)$	Stack after geometry corrections an before range-compression
ϕ_{plon}	Planetographic longitude
$\Psi(p, n)$	Complex-valued signal in the azimuth time and range-time domains
$\Psi_{stack}(b', n')$	Stack after geometry corrections and range compression
$\Psi'_{stack}(b', n')$	Stack after masking
ω	frequency

8 List of acronyms

AGC	Automatic Gain Control
AOCS	Attitude and Orbit Control Subsystem
ATBD	Algorithm Theoretical Baseline Documents
AW	Antenna Weighting File
BW	Bandwidth
BRI	Burst Repetition Interval
CAL1	Calibration Mode 1
CAL2	Calibration Mode 2
C-Band	Secondary Operating Frequency (5.3 GHz) for Jason series altimeters (primarily for measuring ionospheric delay).
CCN	Contract Change Notice
CHD	Characterisation File
CNF	Configuration File
CoM	Centre of Mass
CP4O	Cryosat Plus for Oceans
CryoSat (-2)	ESA altimeter satellite for polar ice investigations
CST	Constants File
CS2	Cryosat-2
DAC	Dynamic Atmospheric Correction
DDM	Delay Doppler Mode
DDP	Delay Doppler Processor
DEM	Digital Elevation Model
DORIS	Doppler Orbitography and Radiopositioning Integrated by Satellite - Orbit determination system.
ECEF	Earth Centred Earth Fixed
EM	Electro-Magnetic
ESA	European Space Agency
EUMETSAT	European Organisation for the Exploitation of Meteorological Satellites
FAI	Fine range word
FBR	Full Bit Rate
FFT	Fast Fourier Transform
FDM	Fast Delivery Marine Product (CryoSat-2 Product)
GIM	Global Ionosphere Maps (source of Ionospheric correction for range)
GNSS	Global Navigation Satellite System
GPP	Ground Prototype Processor
HPBW	Half Power Beam Width
IODD	Input Output Definition Document
IPFDB	Instrument Processing Facility Data Base
I/Q	In-phase (real) and Quadrature (imaginary)
isardSAT	isardSAT, SCOOP Partner
Jason-1, Jason-2	Radar Altimeter Satellites

Jason-CS, Sentinel-6	Joint US / European Radar Altimeter Satellite mission. CS stands for Continuity of Service.
Ku-Band	Primary altimeter operating frequency for most satellite altimeters (13.575 GHz for CryoSat-2)
L0	Level zero (instrument telemetry)
L1A	Level 1A
L1B	Level 1B
L2	Level 2
LAI	Coarse range word
LPF	Low-Pass Filter
LRM	Low Rate Mode
LSE	Least Squares Estimation
LUT	Look Up Table
MDT	Mean Dynamic Topography
MLE	Maximum Likelihood Estimation
MSE	Mean Square Error
MSL	Mean Sea Level
MSS	Mean Sea Surface, Mean Square Slope
NetCDF	(Network common data form) – Set of software libraries and (self - describing, machine independent) data formats.
NOAA	National Oceanic and Atmospheric Administration
NOC	National Oceanography Centre (Southampton, UK)
OSV	Orbit State Vector
PDFsea	Sea Surface Height Probability Distribution Function
PLRM	Pseudo Low Resolution Mode
POCCD	Processing Options Configuration Document
PRF	Pulse Repetition Frequency
PRI	Pulse Repetition Interval
PSD	Product Specification Document
PTR	Point Target Response
RADS	Radar Altimeter Data System (NOAA/TUDelft/EUMETSAT)
RDSAR	Reduced resolution SAR mode data (used to generate PLRM)
RMC	Range Migration Correction
RMS	Root Mean Square
ROI	Region of Interest
SAMOSa	SAR altimetry Mode Studies and Applications
SAR	Synthetic Aperture Radar
SARIN	SAR interferometric mode
SARM	SAR Mode
SatOC	Satellite Oceanographic Consultants
Sentinel-3	ESA Remote sensing mission in the Copernicus programme
Sigma0	Radar Backscatter at nadir
SNR	Signal to Noise Ratio
SPW	Surface Weighting File
SRAL	Synthetic Aperture Radar Altimeter on Sentinel-3

SSH	Sea Surface Height
SSH	Sea Surface Height Anomaly
STARLAB	SCOOP Partner
SWH	Significant Wave Height
TAI	International Atomic Time (from Temps Atomique International)
TN	Technical Note
TUDeft	Delft University of Technology
USO	Ultra Stable Oscillator
UTC	Universal Time Corrected